UNIVERSITY
OF CRETE

Photodissociation of CH$_2$Br$_2$ & CHBr$_3$ at 242nm

Submitted by:

Nektarios Findrilis

Thesis submitted to the Department of Physics for partial
fulfillment of the requirements for the award of the degree of Master of Science

Committee members:

Petros Samartzis   Peter Rakitzis   Iannis Kominis

IESL   Physics Department   Physics Department

FORTH   University of Crete   University of Crete

July 2023

Dedicated to my family,

Ioulia Zacharia

Emmanuel Findrilis

Sophia Findrili

TABLE OF CONTENTS

ACKNOWLEDGMENTS

1

ABSTRACT

The UV photochemistry of bromine-containing molecules has been the subject of significant attention due to their contribution to stratospheric ozone depletion by bromine radicals. In this work, we investigated the photodissociation dynamics of dibromomethane (CH_2Br_2) and bromoform ($CHBr_3$) using Velocity Map Imaging (VMI) at 242nm. By analyzing the nascent photoelectron and photofragment images e.g., C^+, Br^+, CH^+, and their kinetic energy release distribution we identified active photoexcitation and photodissociation pathways for each molecule.

2

ΠΕΡΙΛΗΨΗ

Η υπεριώδης φωτοχημεία μορίων που περιέχουν βρώμιο έχει τραβήξει σημαντική προσοχή λόγω της συμβολής τους στην μείωση του στρατοσφαιρικού όζοντος από τις ρίζες βρωμίου. Σε αυτήν την εργασία, διερευνήσαμε τη δυναμική φωτοδιάσπασης του διβρωμομεθανίου (CH_2Br_2) και του βρωμοφορμίου ($CHBr_3$) χρησιμοποιώντας την τεχνική απεικόνισης ταχύτητας ιόντων (VMI) στα 242nm. Αναλύοντας τις εικόνες των νεοσχηματιζόμενων φωτοθραυσμάτων, όπως C^+, Br^+, CH^+, και την κατανομή της κινητικής τους ενέργειας, καθώς και των φωτοηλεκτρονίων, εντοπίσαμε τις ενεργές διαδρομές φωτοδιέγερσης και φωτοδιάσπασης για κάθε μόριο.

Chapter 1 Introduction

1.1 Molecular Reaction Dynamics

Molecular reaction dynamics is the study of the atomic-level mechanisms (forces) that drive chemical reactions. The study of those elementary processes aims to find the means of probing, understanding, and controlling chemical reactions[1]. The insights obtained through the study of molecular reaction dynamics enable a deeper understanding of established processes, uncovering novel mechanisms, and driving technological advancements.

In this thesis, we will concentrate on two of the simplest, yet fundamental processes, ionization, and photodissociation or photolysis, that play a pivotal role in numerous physical and chemical phenomena.

1.1.1 Potential Energy Surfaces

Potential Energy Surfaces (PES) describe the energy of a system, especially a collection of atoms. Energy is defined as a function of one or more coordinates, one for each degree of freedom. If there is only one coordinate, e.g., diatomic molecules, it is called an energy curve. The set of coordinates could be the Cartesian coordinates of the atoms or a set of inter-atomic distances and angles.
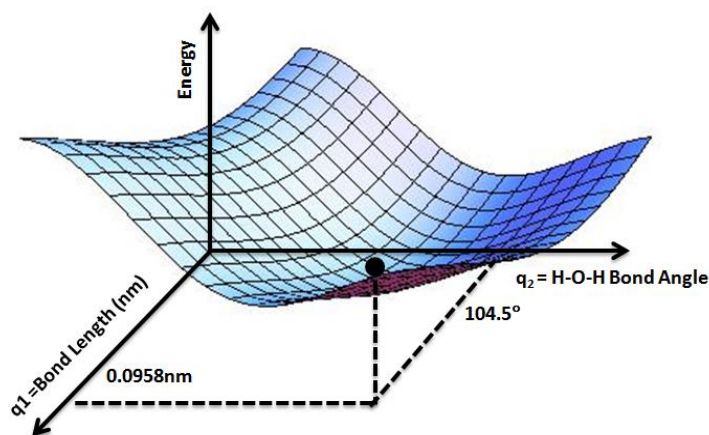
Figure 1.1 PES of H_2O: 2 degrees of freedom, one for each bond. This figure is sourced from Wikipedia (https://en.wikipedia.org/wiki/Potential_energy_surface).

PES is a conceptual tool for aiding the analysis of molecular geometry and reaction dynamics. All necessary information can be depicted on the PES, such as the bond lengths and angles, the bond energy, the chemical reaction mechanism, the kinetic and internal energy of the reactants and the products, and how the system changes with the relative position of the atoms.

1.1.2 Photodissociation

When a molecule absorbs light (photons) many processes can occur, such as excitation to an excited state, internal energy redistribution, phosphorescence[2], fluorescence[2], ionization, and photodissociation. The molecule's dissociation is determined by the energy of the photon/s and, more importantly, the shape of the PES of the excited state. Based on their shape, PES can be classified as attractive and repulsive. An attractive state is a bound electronic state of the molecule, with a minimum of potential energy at a finite distance between atoms, i.e., the bond length. A repulsive state lacks such minima and results in the molecule's dissociation.
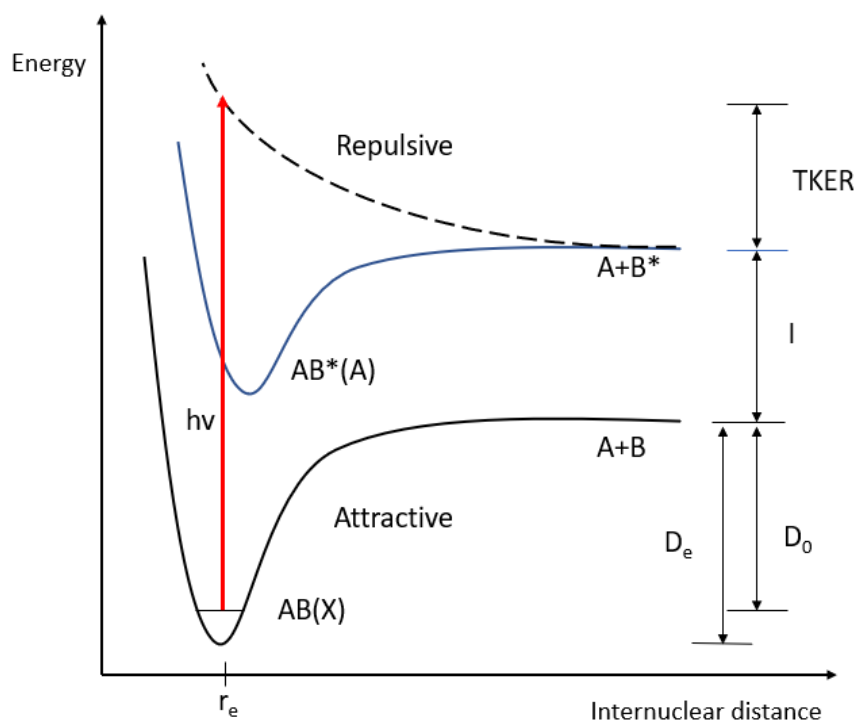
Figure 1.2 Photodissociation of a diatomic molecule depicted on an energy curve.

As seen in the figure above, during the photodissociation process, a part of the photon's energy is consumed to break the molecule's bond, and the rest is distributed as internal energy (I) and kinetic energy (T) of the photofragments. Due to the law of conservation of energy:

$$E_i(AB) + hv = D_0 + I(A) + T(A) + I(B^*) + T(B^*) \qquad 1.1$$

Where $E_i(AB)$ is the initial energy of the molecule and D_0 is the bond dissociation energy. Moreover, the sum of the photofragments' kinetic energy equals the Total Kinetic Energy Release (TKER) by the photodissociation process:

$$TKER = T(A) + T(B^*) = \frac{1}{2}m_A u_A^2 + \frac{1}{2}m_B u_B^2 \qquad 1.2$$

Where m_A and m_B are the masses of the photofragments A and B respectively.

In the upcoming subchapters, we will examine the internal and kinetic energy of the photofragments in detail, along with their angular distribution.

1.1.3 Internal Energy of Molecules

A molecule can absorb energy from its surroundings as internal energy through various processes, including mechanical work, chemical reactions, heat transfer, and absorption of light. The acquired internal energy is subsequently distributed among the molecule's internal degrees of freedom, which are rotational, vibrational, and electronic energy levels. In contrast, an atom possesses only electronic states. This subsection provides information about these internal degrees of freedom, aiming to establish a foundational understanding, particularly focusing on the case of diatomic molecules.

Starting from the degrees of freedom with the smallest energy, the rotation of a diatomic molecule can be illustrated by the classical rigid rotor model[3,4]:
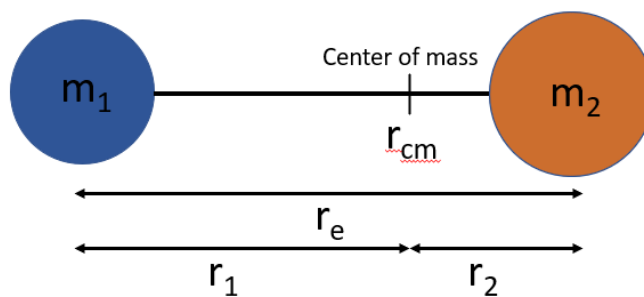
Figure 1.3 The rigid rotor

Where m_1 and m_2 are the masses of the atoms that form the molecule and r_1 and r_2 are the nuclear distances from the center of mass of the atom 1 and 2 respectively. The center of mass is defined as:

$$m_1 r_1 = m_2 r_2 \quad\quad\quad 1.3$$

The classical expression for the energy of the system shown in Figure 1.3, rotating about an axis (z) is:

$$E = \frac{1}{2}I\omega^2 = \frac{J^2}{2I} \quad\quad\quad 1.4$$

Where ω is the angular frequency, I is the moment of inertia and $J=I\omega$ is the angular momentum of the rigid rotor. The moment of inertia is defined as:

$$I = \frac{m_1 m_2}{m_1 + m_2} r_e^2 = \mu r_e^2 \quad\quad\quad 1.5$$

Where μ is the reduced mass of the system.

In quantum mechanics, the Hamiltonian of a system equivalent to the one depicted in Figure 1.3 is given by the equation:

$$\hat{H} = \frac{\hat{J}^2}{2I} \quad\quad\quad 1.6$$

The corresponding eigenvalues of the Hamiltonian are:

$$E_J = \frac{\hbar^2}{2I}J(J+1) = hcBJ(J+1) \quad\quad\quad 1.7$$

Where J represents the angular momentum quantum number, taking positive integer values ($J=0$, 1, 2…), and $B = \frac{\hbar}{4\pi cI}$ is referred to as rotational constant. The energy of a rotational state is normally reported as the rotational term, $F(J)$, a wavenumber, by division by hc:

$$F(J) = BJ(J+1) \quad\quad\quad 1.8$$

The atoms of a rotating diatomic molecule are subject to centrifugal forces, which tend to stretch the bond and hence increase the moment of inertia. This effect is considered by subtracting a term from the energy, writing:

$$F(J) = BJ(J+1) - D_J J^2(J+1)^2 \quad\quad\quad 1.9$$

Equation 1.9 gives the energy of a rotational state of the nonrigid rotor model. The parameter D_J is called the centrifugal distortion constant and is equal to $\frac{4B^3}{\omega}$, where ω is the vibration wavenumber of the bond (a measure of the bond's stiffness). The second term becomes significant for high values of J and can often be neglected.

In general, the rotational properties of any polyatomic molecule can be expressed in terms of the moments of inertia about a set of three perpendicular axes. These moments of inertia are labeled as I_a, I_b, and I_c, with the convention that $I_c > I_b > I_a$. Rigid rotors can be categorized into four groups:

- Spherical rotors (3 equal moments of inertia)
- Symmetric rotors (2 equal moments of inertia)
- Linear rotors (1 moment of inertia in total, i.e. diatomic molecules)
- Asymmetric rotors (3 different moments of inertia)

Similarly, our discussion of the vibrational motion of a diatomic molecule will begin with the classical case, in which the system shown in Figure 1.3 undergoes vibration and the two masses are displaced from their equilibrium positions. For very small displacements, $x=r-r_e$, we can expand the potential energy of the system around its minimum (at the equilibrium position) by using a Taylor series:

$$V(x) = V(0) + \left(\frac{dV}{dx}\right)_0 x + \frac{1}{2}\left(\frac{d^2V}{dx^2}\right)_0 x^2 + \cdots \qquad 1.10$$

The term $V(0)$ can be set arbitrarily to zero. Furthermore, the first derivative of V is zero at the minimum. Therefore, the first surviving term gives a parabolic potential, known as the harmonic oscillator potential[3,4]:

$$V(x) = \frac{1}{2}kx^2 \qquad 1.11$$

Where $k=\left(\frac{d^2V}{dx^2}\right)_0$, and it is called the force constant. Solving the time-independent Schrödinger equation with the potential of the harmonic oscillator yields the energy eigenvalues:

$$E_v = (v + \frac{1}{2})\hbar\omega \qquad 1.12$$

Where $\omega = \sqrt{\frac{k}{m_{eff}}}$ is the vibrational frequency of the system, $m_{eff} = \frac{m_1 m_2}{m_1 + m_2}$ is the effective mass, and v denotes the vibrational quantum number, which takes positive integer values ($v = 0, 1, 2..$). The eigenvalue E_0 ($v = 0$) is called zero-point energy.

As previously mentioned, the harmonic oscillator potential provides an approximation of the true diatomic molecule's potential energy curve close to the minimum (like the attractive electronic state shown in Figure 1.2). However, due to the confining parabolic form of the harmonic oscillator potential energy, dissociation becomes impossible. Therefore, higher-order terms of the Taylor series should be considered, leading to anharmonic motion and a better approximation of the molecule's potential energy, known as the Morse potential energy[3]:

$$V(r) = D_e\{1 - \exp(-a(r - r_e))\}^2 \qquad 1.13$$

Here, D_e represents the depth of the potential minimum, and $a = \left(\frac{m_{eff}\omega^2}{2hcD_e}\right)^{1/2}$ measures the curvature at the bottom of the potential well.

Solving the Schrödinger equation for the Morse potential yields the energy eigenvalues:

$$E_v = \left(v + \frac{1}{2}\right)\hbar\omega - \left(v + \frac{1}{2}\right)^2 \hbar x_e \omega \qquad 1.14$$

Where x_e is called the anharmonicity constant.

The bond dissociation energy, D_0, is related to the depth of the potential minimum using the equation:

$$D_0 = D_e - E_0 = D_e - \frac{1}{2}\hbar\omega - \frac{1}{4}\hbar x_e \omega \qquad 1.15$$

Figure 1.4 is a schematic representation of the Morse potential, as well as the rotational and vibrational energy levels of a diatomic molecule.

Diatomic molecules have only one mode of vibration, the bond stretch, with energy levels discussed above. On the other hand, polyatomic molecules exhibit several modes of vibration, as alterations in bond lengths and angles become possible. Specifically, non-linear polyatomic

molecules have 3N-6 independent vibrational modes, where N represents the molecule's atom count, whereas linear molecules have 3N-5.
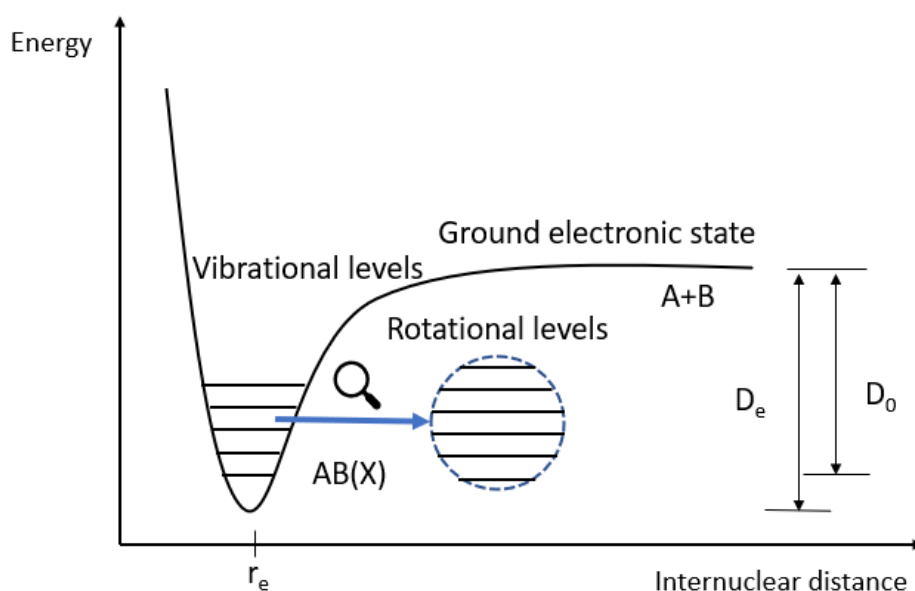
Figure 1.4 Potential energy curve of a diatomic molecule's ground state, including the representation of vibrational and rotational energy levels.

1.1.4 Term Symbols and Selection Rules

An electronic state is defined by the electron configuration of the atom or molecule and by the quantum numbers of each electron contributing to the configuration. A term symbol is an abbreviated description of the total spin (S), total orbital angular momentum (L), and total angular momentum (J) quantum numbers of an atomic electronic state.

The usual term symbol assumes L-S coupling scheme[5], and has the notation:

$$^{2S+1}L_J \qquad\qquad 1.16$$

Where $2S+1$ represents the spin multiplicity, and L is indicated using the spectroscopic notation "S", "P", "D", "F", … representing $L=0, 1, 2, 3,$ … respectively. To determine the term symbol that corresponds to the ground state, we employ a set of rules known as Hund's rules[6].

Similarly, a molecular term symbol is an abbreviated description of a molecular electronic state and applies to homonuclear diatomic molecules, or symmetric molecules with an inversion center.

It has the notation:

$$^{2S+1}\Lambda_{\Omega,(g/u)}^{(+/-)}$$ 　　　　1.17

Where:

- $2S+1$ denotes the spin multiplicity,
- Λ is the projection of the total orbital angular momentum along the internuclear axis. It is written using the spectroscopic notation "Σ", "Π", "Δ", "Φ", … to represent $\Lambda=0, 1, 2, 3,$ … respectively,
- Ω is the projection of the total angular momentum along the internuclear axis,
- g/u represents the symmetry of parity with respect to inversion (i) through a center of symmetry,
- +/- signifies the reflection symmetry along an arbitrary plane containing the internuclear axis, for Σ states ($\Lambda=0$).

When the atom/ molecule interacts with an electromagnetic wave (light), it induces an electromagnetic moment. If the frequency of the induced moment matches the energy difference between the initial (i) and the final (f) state, divided by $\hbar$, the interaction is considered resonant. The transition moment refers to the amplitude of the electromagnetic moment, with the electric dipole transition being the most significant.

The condition for an electric dipole transition to occur is the following:

$$\vec{\mu}_{fi} = -e \int \psi_f^*(\vec{r})\vec{r}\psi_i(\vec{r})d^3\vec{r} \neq 0$$ 　　　　1.18

Where $\vec{\mu}_{fi}$ is the transition dipole moment. If the condition is satisfied, the transition is allowed; otherwise, it is forbidden. Equation 1.18 leads to the derivation of selection rules for electronic transitions.

The atomic selection rules are presented in the following table[5]:

ΔL	ΔS	ΔJ	Δl
0, ±1	0	0, ±1 J=0←|→J=0	±1

Table 1.1 Selection rules of atomic electric transitions.

Where l is the orbital angular momentum quantum number of the electron. The symbol "←\|→" indicates a forbidden transition.

Respectively, the molecular selection rules, based on Hund's coupling case (a)[7], are presented in the following table:

ΔΛ	ΔΣ	ΔΩ	ΔJ	g/u	±
0, ±1	0	0, ±1	0, ±1	u↔g	+↔-

Table 1.2 Selection rules of molecular electric transitions.

Where $\Delta\Sigma$ is the projection of the total angular momentum along the internuclear axis.

1.1.5 Kinetic Energy Release and Angular Distribution

We consider the photodissociation process described by Equation 1.1. Within the molecular frame, momentum conservation yields the following relationship:

$$m_A u_A = m_B u_B \qquad\qquad 1.19$$

By combining equations 1.2 and 1.19 we obtain:

$$T(A) = \frac{m_B}{M} TKER, \quad T(B^*) = \frac{m_A}{M} TKER \qquad\qquad 1.20$$

Here, $M = m_A + m_B$. Therefore, by measuring the kinetic energy of one photofragment, we can determine the kinetic energy (speed) of the other fragment and the TKER.

When multiple dissociation events occur, each event produces photofragments with the same speed but in different directions. The accumulation of these events results in a spherical distribution in velocity space known as Newton spheres (velocity spheres) [8], as depicted in Figure 1.5. The size of a Newton sphere is directly proportional to the speed of the fragment (a scalar quantity), and the surface pattern reveals the angular distribution of the photodissociation (directionality).
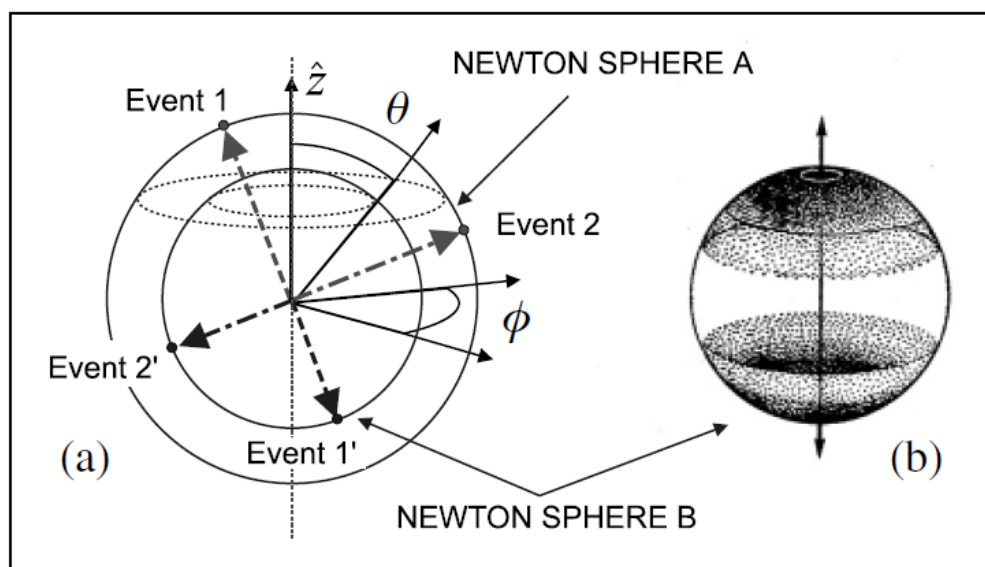

Figure 1.5 **(a)** A pair of Newton spheres with spherical coordinates r (not shown), θ, and φ, where r id the sphere radius, θ is the polar angle with respect to the z axis, and φ is the azimuthal angle. Two events are shown in **(a)** with equal and opposite momentum. **(b)** By summing up many events (here for particle B), a surface pattern emerges as shown. Most of the surface intensity of this example is at the poles, representative of a typical $\cos^2\theta$ distribution. This figure is sourced from the ref [8].

Having examined the speed aspect, it is essential to explore the directional patterns inherent in the angular distribution of the fragment's recoil velocity after the photodissociation process.

When utilizing linear polarized light to induce photodissociation in a collection of parent molecules, the electric field vector $\vec{\varepsilon}$ defines a fixed direction in the laboratory frame. Thus, all vectors inherent to the photodissociation process can be measured relative to the polarization axis of the dissociating electric field. In this context, the vectors of significance are the transition dipole moment of the parent molecule, $\vec{\mu}_{fi}$, and the recoil velocity of the fragments, $\vec{v}$.

The orientation of $\vec{\mu}_{fi}$ in relation to $\vec{\varepsilon}$ can vary randomly across the assembly of parent molecules. As light absorption occurs through the interaction between $\vec{\mu}_{fi}$ and $\vec{\varepsilon}$, the probability of absorption is proportional to the magnitude of $\left|\vec{\mu}_{fi}\vec{\varepsilon}\right|^2$. Consequently, a selective absorption takes place,

preferentially exciting and dissociating parent molecules whose transition dipole moment aligns parallel to $\vec{\varepsilon}$, resulting in an anisotropic angular distribution.

Moreover, when $\vec{\mu}_{fi}$ aligns with the laboratory frame defined by $\vec{\varepsilon}$, assuming rapid dissociation process, the recoil velocity $\vec{v}$ also aligns with the laboratory frame. For example, in the case of diatomic molecules, $\vec{v}$ will be either parallel or perpendicular to $\vec{\mu}_{fi}$.

Zare was the first to highlight that the vector correlation between the parent's transition dipole moment and the product's velocity can lead to an anisotropic distribution of the photofragments[9]. He also noted that, for a diatomic parent molecule, the normalized angular distribution of the photofragments can be described by the following equation[10]:

$$I(\theta) = \frac{1}{4\pi}[1 + \beta P_2(cos\theta)] \qquad 1.21$$

Where β is the anisotropy parameter, taking values: $-1 \leq \beta \leq 2$. Also, P_2 refers to the second-order Legendre polynomial $(P_2(x) = \frac{1}{2}(3x^2 - 1))$ and θ is the angle between $\vec{\varepsilon}$ and $\vec{v}$.

The extreme values of β can provide valuable information regarding the symmetry of the electronic states involved in the parent molecule's dissociation. For example, when $\beta = 2$, the anisotropy of $I(\theta)$ follows $cos^2(\theta)$ distribution, peaking at $\theta = 0$. This indicates that the fragments recoil along $\vec{\varepsilon}$, as expected for excited states of the parent molecule with Λ (or $\Delta\Omega$) = 0, e.g. Σ states, with $\vec{\mu}_{fi}$ aligned parallel to the molecular axis (parallel transition). Conversely, for $\beta = -1$, the anisotropy follows a $sin^2(\theta)$ distribution, peaking at $\theta = \pi/2$, indicating involvement of states with Λ (or $\Delta\Omega$) = 1 e.g. Π states, where $\vec{\mu}_{fi}$ aligns perpendicular to the molecular axis (perpendicular transition). The case of $\beta = 0$ corresponds to an isotropic distribution, where the dissociation occurs independently of the angle θ, resulting in isotropically distributed fragments.

For multiphoton transitions, higher-order Legendre polynomials are needed. In general:

$$I(\theta) \propto \sum_n a_{2n} P_{2n}(cos\theta) \qquad 1.22$$

Moreover, the case for polyatomic molecules is somewhat more complicated. Assuming rapid photodissociation limit, then the anisotropy parameter can be determined by the equation:

$$\beta = 2P_2(cosa) \qquad 1.23$$

Where a represents the angle between $\vec{\mu}_{fi}$ and the breaking bond in the molecule.

1.1.6 Ionization and Multi-photon Ionization

Ionization is a phenomenon that occurs when a molecule absorbs enough energy to surpass the Ionization Potential (IP) threshold. If the excitation is caused by the absorption of photons, it is called photoionization. The reaction proceeds as follows:

$$AB + nhv \rightarrow AB^* \rightarrow AB^+ + e^-$$ 1.24
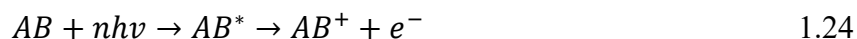
Given that the mass of the electron is much smaller than that of the molecule, it is reasonable to assume that the electron absorbs almost all the access energy $(E(nhv) - IP)$ as kinetic energy and the molecule's velocity remains constant.

Since the IP of most small molecules is above $8eV$[11], highly energetic photons are required to induce photoionization through a Single-Photon Ionization (SPI), produced by expensive synchrotron sources[12]. When laser sources with high photon flux ($\#photons\ cm^{-2}\ s^{-1}$) are utilized, simultaneous absorption of multiple photons can occur to surpass the IP. This phenomenon is called Multi-Photon Ionization (MPI) and enables the ionization of small molecules in the near ultraviolet-visible region. The likelihood of MPI occurrence decreases as the number of photons required to exceed the IP increases.

The importance of state selectivity in the investigation of photoionization phenomena cannot be overstated. The Resonance Enhanced Multi-Photon Ionization (REMPI) method is the most widely used MPI technique due to its ability to provide state-selective ionization. REMPI involves two steps: resonant excitation to an intermediate state, followed by ionization. Depending on the molecule under investigation, different REMPI schemes can be employed, such as the one-color scheme (using photons of the same frequency for both steps) and the two-color scheme (using photons of different frequencies). The notation for these schemes is (n+m) REMPI and (n+m') REMPI respectively. The probability of REMPI occurrence is significantly higher than that of non-resonance excitation due to the resonance of the n photons' energy with the difference between the ground and the excited state. Thus, REMPI provides state selectivity.

All ionization phenomena described above are depicted in the following figure:
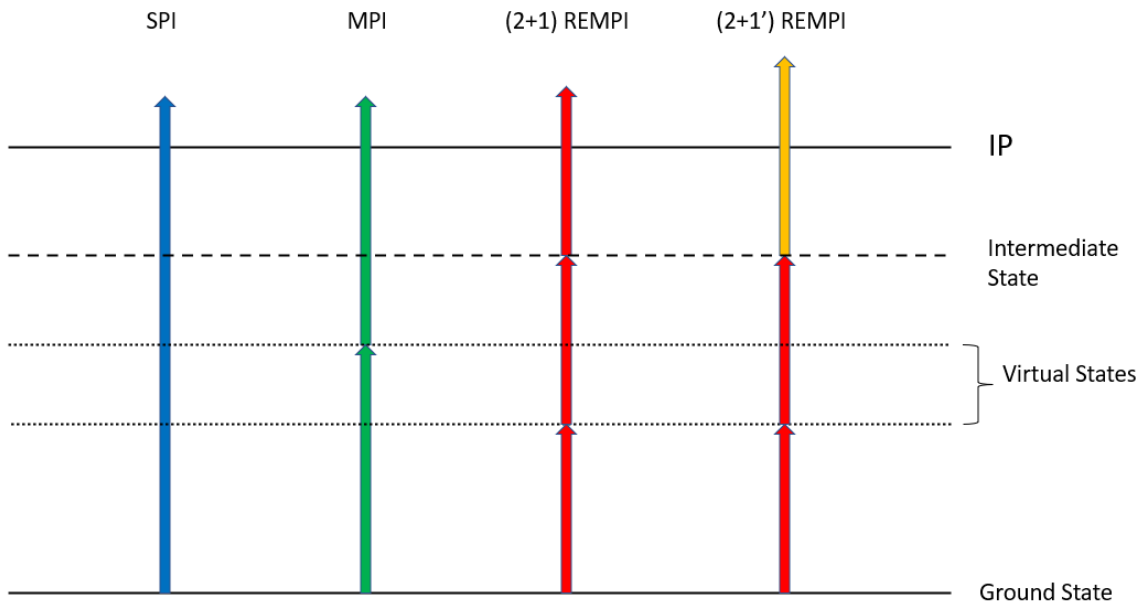
Figure 1.6 SPI, MPI and REMPI. A virtual state is a not physically realizable energy state used as an intermediate state for multi-photon phenomena.

1.1.7 Molecular beams

The free-jet molecular beam is a neutral beam extracted from an underexpanded, supersonic, continuum jet expansion from a high-pressure gas source into a low-pressure ambient background[13]. Figure 1.7 provides a schematic representation of this expansion process under continuum conditions.

Figure 1.7 Continuum free-jet expansion. The figure is sourced from ref [13]

Initially, the gas inside the reservoir is in a low kinetic energy state known as the stagnation state, with pressure P_0 and temperatur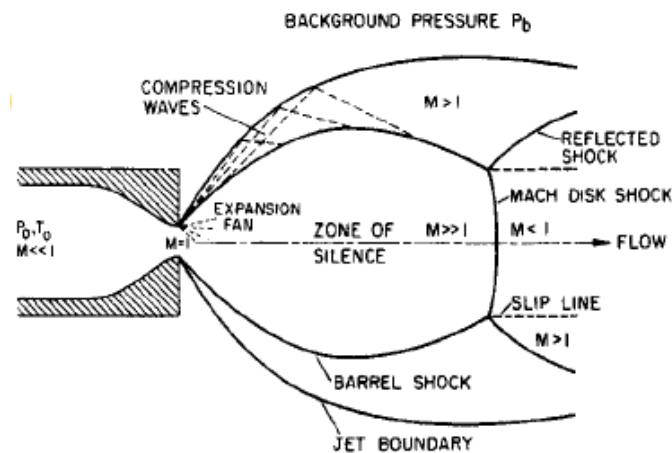e T_0. It then passes through an orifice (nozzle) with a diameter comparable to the collision mean free path and exits into a low-pressure region (vacuum chamber) due to the pressure difference (P_0- P_b), where P_b is the background pressure of the chamber.

The speed of the gas flow can be subsonic (lower than the local speed of sound), sonic (equal to the local speed of sound), or supersonic (greater than the speed of sound. The Mach number (M) defines the ratio of the mean gas's speed to the speed of sound, where:

- M<1 indicates subsonic flow,
- M=1 indicates sonic flow,
- M>1 indicates supersonic flow.

The gas speed and its behavior upon exiting the nozzle depends on the ratio $\frac{P_0}{P_b}$, particularly if it exceeds a critical value given by equation 1.25:

$$G = \left(\frac{\gamma+1}{2}\right)^{\frac{\gamma}{\gamma-1}}$$
1.25

Here, γ represents the adiabatic index or the ratio of specific heat capacities ($\frac{C_p}{C_v}$) for the gas. The value of G is always less than 2.1 for all gases.

If the pressure ratio $\frac{P_0}{P_b}$, is less than G, the flow is subsonic, and the exit pressure approximately equals P_b. If the ratio is greater than G, then M=1. In this case, the exit pressure of the flow does not depend on the background pressure and is equal to $\frac{P_0}{G}$, a value larger than P_b, and the flow is called "underexpanded". The flow then undergoes further expansion upon exiting the nozzle, influenced by boundary conditions created by the P_b. During the expansion, M increases and becomes greater than 1 (supersonic flow). Then, information propagates at a lower speed than the flow itself. Therefore, the flow is unaware of the boundary conditions (P_b and M outside the nozzle).

Shock waves are disturbances that propagate faster than the local speed of sound and exhibit regions with different pressure, temperature, density, and velocity gradients. These shock waves reduce the velocity of the flow, transitioning it back to a subsonic state. Consequently, the flow can adjust to the boundary conditions. Figure 1.7 illustrates compression waves, reflected shock,

Mach disk shock, and barrel shock. The barrel shock compresses the flow at the sides, while the Mach disk shock occurs at the centerline.

The region referred to as the "zone of silence" corresponds to the central area of the flow where conditions are isentropic, and influences of viscosity and heat conduction are negligible. The Mach number is significantly greater than 1, implying that the zone of silence is unaware of the external conditions.

Utilizing this specific part of the molecular beam is advantageous, which is why a device called a skimmer is employed to capture it before it collapses into the Mach disk. A skimmer consists of a truncated cone-shaped aperture designed to allow molecules traveling along the beam axis to pass through while deflecting molecules that deviate from the central axis. The skimmer should be positioned ahead of the Mach disk location. The distance (x_m) of the Mach disk from the nozzle can be calculated using the following formula:

$$\frac{x_m}{d} = 0.67 \left(\frac{P_0}{P_b}\right)$$
<div align="right">1.26</div>

Where d is the diameter of the nozzle.

1.2 Ion Imaging

In molecular reaction dynamics, numerous problems necessitate the simultaneous measurement of both the speed and angular direction of the particles involved. Among these problems, the most demanding ones involve the measurement of particles' velocity in coincidence with their internal energy[8]. Photodissociation processes are prominent examples of such challenges, as a complete understanding of these processes can only be achieved when the internal energies and velocities of all resulting products are specified.

Ion imaging serves as a valuable multiplex detection technique to address these challenges. It enables the simultaneous measurement of the photofragments' kinetic energy release, which can be utilized to calculate their internal energy using Equation 1.1, as well as their angular distribution.

Specifically, the Velocity Map Imaging (VMI) technique, employed in the experiments of this thesis, has had a profound impact on the field of molecular dynamics, particularly on the study of photodissociation and state-selective ionization of diatomic and small molecules.

1.2.1 Velocity Map Imaging

Figure 1.8 depicts the entire process of imaging the photodissociation in a molecular beam by means of VMI[14].

Step a) involves the photodissociation of molecules in a skimmed supersonic cold molecular beam using a linearly polarized laser beam. The laser beam is polarized parallel to the z-axis, which aligns with the detector face. The nascent photofragment molecules form concentric Newton spheres which are subsequently ionized by the same laser beam in step b). The Newton sphere of the resulting ions is almost identical to the neutral photofragments' sphere. This similarity arises from the electron absorbing most of the excess energy, as discussed in Section 1.1.6.

The molecular beam-laser interaction occurs between two flat electrodes with circular concentric holes, namely the extractor and the repeller (Figure 1.8 **B**). These electrodes, along with a third ground electrode, produce an electric inhomogeneous lens-like field[15,16], accelerating the produced ion Newton spheres towards a Time of Flight (TOF) tube, and focusing (mapping) nascent ions with the same velocity along the plane parallel to the detection phase onto the same point of the detector, regardless of their origin in the molecular beam-laser interaction volume.
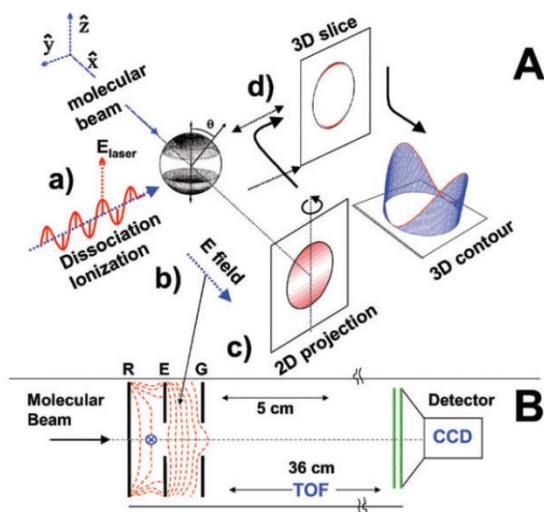

Figure 1.8 Velocity Map Imaging approach of photodissociation.
This figure is sourced from the reference [14].

The TOF tube is a field-free region that allows the separation of different ion fragments' Newton spheres based on their distinct mass-to-charge ratios.

 In step c), the Newton spheres of nascent ions are projected onto a 2D Position-Sensitive Detector (PSD). Consequently, the detected ion distribution is the 2D projection of the true 3D Newton sphere.

By applying an appropriate mathematical transform (inverse Abel transform), given that the 3D Newton sphere shows cylindrical symmetry to the z-axis parallel to the PSD face, we can obtain the central slice of the real ion distribution, as shown in step d). The center slice is displayed in Figure 1.8 **A** both as a 2D diagram and as a 3D contour diagram.

1.2.2 Time of Flight Mass Spectroscopy

As mentioned in the previous section, the concentric Newton spheres of the nascent ion fragments undergo separation based on their different mass-to-charge ratios when they enter the TOF tube.

To illustrate the principle behind this separation, let's consider the example of an ion with mass m and charge $q=ze$, which enters a region with an electric field. In this case, we will use a homogeneous electric field with a potential V. The ion gains additional kinetic energy, given by the equation:

$$E_k = \frac{1}{2}mv^2 = zeV \qquad\qquad 1.27$$

Here v is the additional speed gained by the ion along the TOF axis, due to the acceleration in the electric field region.

By solving Equation 1.27 for the speed v, we obtain:

$$v = \left(\frac{2zeV}{m}\right)^{1/2} \qquad\qquad 1.28$$

Following the acceleration, the ion enters a field-free tube with a length of D. The additional speed gained corresponds to a TOF:

$$t = \frac{D}{v} = \frac{D}{\sqrt{2eV}}\sqrt{\frac{m}{z}} \qquad\qquad 1.29$$

In equation 1.29, the quantity m/z denotes the mass-to-charge ratio. Therefore, ions with different mass-to-charge ratios will exhibit different TOFs as they cross the TOF tube, resulting in their spatial separation.

1.2.3 Inverse Abel Transform

In image analysis, the inverse Abel transform[17] is used to calculate a 3D axially symmetric distribution from its projection on a 2D plane. If we consider $F(y)$ as the function representing a horizontal slice of the 2D projection, and $f(r)$ as the function representing a horizontal circular slice of the detected Newton's sphere, then we can obtain $f(r)$ from $F(y)$ from the inverse Abel transform, which is expressed by the following equation:

$$f(r) = -\frac{1}{\pi} \int_r^\infty \frac{dF(y)}{dy} \frac{dy}{\sqrt{y^2 - r^2}}$$ 1.30

Likewise, $F(y)$ can be obtained from $f(r)$ using the Abel transform, given by the equation:

$$F(y) = 2 \int_y^\infty \frac{f(r)r}{\sqrt{r^2 - y^2}} dr$$ 1.31

Figure 1.9 illustrates a schematic representation of both the Abel and the inverse Abel transform.
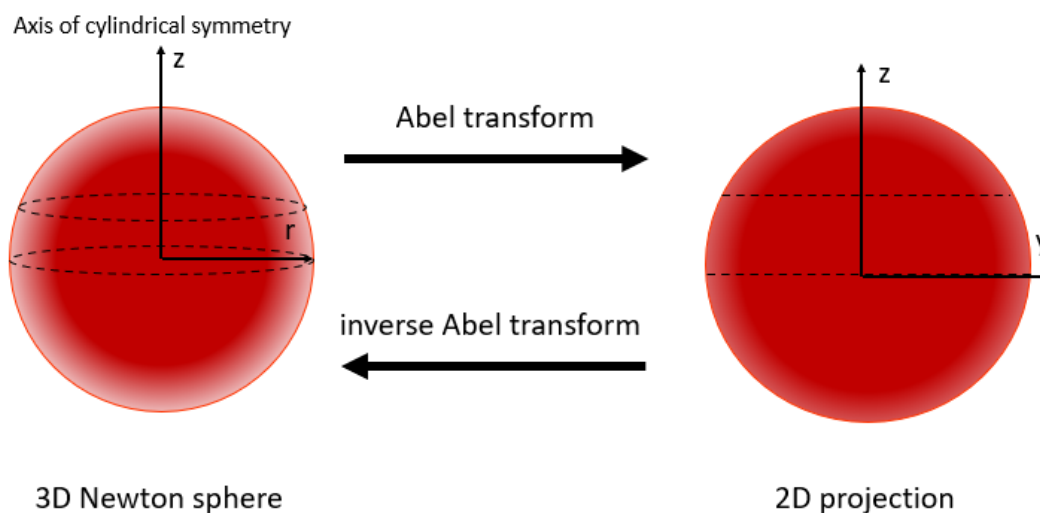

Figure 1.9 A schematic representation of the Abel and inverse Abel transform.

1.2.4 Ion Imaging History

Ion imaging, first demonstrated by Chandler and Houston in their pioneering study in 1987[18], has paved the way for advancements in the field of molecular reaction dynamics. Their first imaging experiment was the photodissociation of methyl iodine (CH_3I), where the three-dimensional velocity distribution of the nascent fragments was accelerated and projected to a Position Sensitive Detector (PSD) using a homogeneous electric field, generated by a repeller and two grounded grid

electrodes. The reconstructed three-dimensional Newton sphere of the nascent CH_3^+ ions was obtained through the application of inverse Abel transform to the two-dimensional projection.

Although Chandler and Houston's research showcased the effectiveness of ion imaging, the energy resolution was limited to 15% because of the finite size of the molecular beam-laser interaction volume. Consequently, photodissociation occurs at various positions within the molecular beam, leading to spatial dispersion that causes image blurring.

Significant improvement in energy resolution within the field of ion imaging was achieved by Eppink and Parker in 1997 with the introduction of the VMI technique[19]. The VMI setup involved an acceleration region incorporating three flat electrodes with circular concentric holes, the repeller, the extractor, and the ground, that act as an electrostatic lens (inhomogeneous field). By adjusting the relative voltage between the repeller and the extractor, ions with similar velocities (in a direction parallel to the imaging plane) focus on a common point on the imaging plane, regardless of where they originated in the molecular beam-laser interaction volume. This breakthrough led to an improvement in energy resolution, ranging from 2% to 5%.

A further advancement came with the introduction of slice imaging by Gebhardt *et al.* in 2001[20]. This technique eliminated the need for the inverse Abel transform. This was achieved by using a delayed pulsed extraction of ions following dissociation, which resulted in a velocity spread of the ion distribution. Subsequently, a narrow electrical detector-gating pulse could extract and image the central slice of the ion cloud directly from the three-dimensional spatial distribution of photofragments. Slice imaging not only allowed the imaging and analysis of non-cylindrical symmetric distributions but also enhanced the sensitivity by avoiding the blurring associated with the inverse Abel transform.

Over the years several other improvements and variations of the Slice imaging technique have been published, including direct current slice imaging[21], and slice imaging using a single field[22]. These advancements have further enhanced the versatility of the Slice Imaging technique in studying molecular reaction dynamics.

Chapter 2 Experimental apparatus

The apparatus used for the experiments of Chapter 3 and Chapter 4 is shown in Figure 2.1[23]. Its parts will be discussed in the following subchapters.
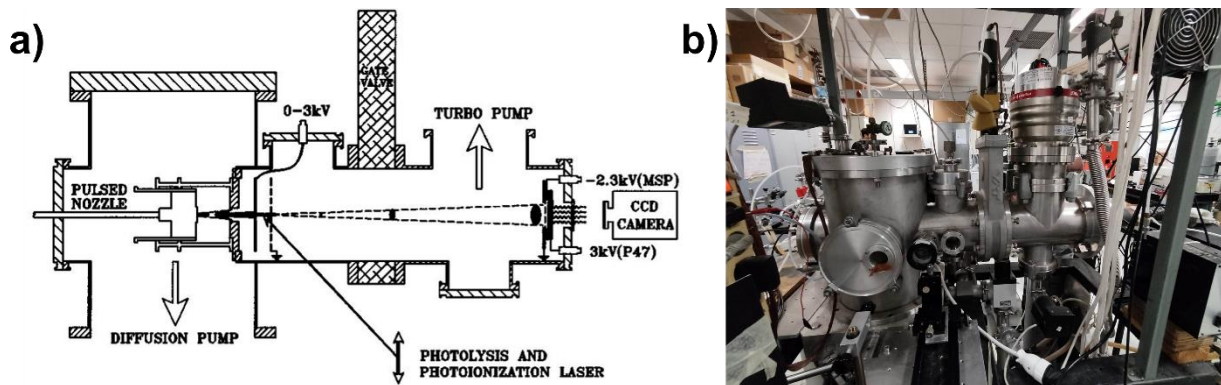

Figure 2.1 VMI apparatus, **a)** 2D representation sourced from reference [23], **b)** photograph.

2.1 Source Chamber

The first vacuum chamber of the VMI apparatus is called the source chamber, and it serves as the location where the molecular beam is generated through a nozzle. This chamber is maintained at a pressure of ~10^{-6}mbar, achieved by utilizing a baffled oil diffusion pump (Leybold DI3000, 3000lt/sec). Assisting the diffusion pump is a rotary mechanical oil pump (Leybold Trivac D65B, 65m^3/h), which provides a backing pressure of ~10^{-3}mbar. The source chamber and the second vacuum chamber, the detection chamber, are separated by a skimmer (∅=1.5mm), which serves as the differential pumping point between the two chambers.

2.2 Nozzle

The molecular beam is generated by expanding the gas mixture through a nozzle, transitioning from the stagnation state to the source chamber. The nozzle used is a home-made pulsed valve, which is piezoelectrically actuated and based on the design by Proch and Trickl[24]. It has an aperture size of $\emptyset$= 0.8mm. To operate the piezoelectric crystal, a pulse voltage of 800V is applied at a repetition rate of 10Hz. The positioning of the nozzle ensures that its aperture is located ~1-2cm away from a skimmer, keeping the zone of silence of the gas flow. The nozzle and the skimmer are depicted in the figure below:
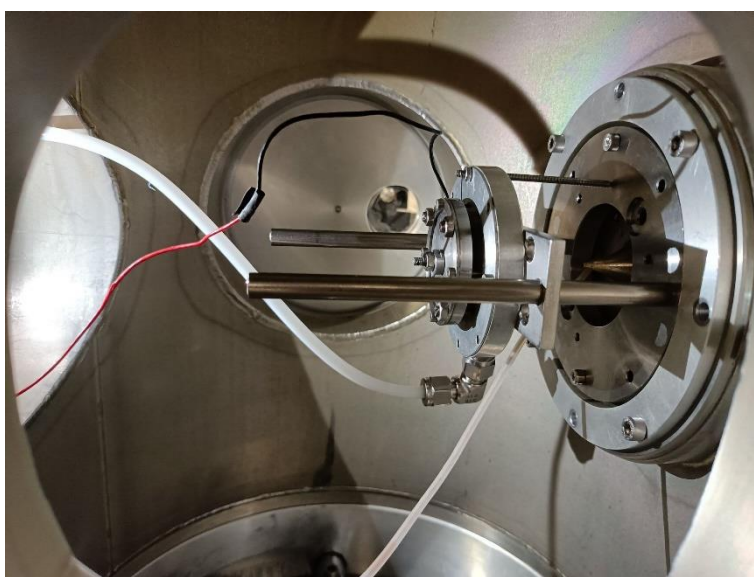

Figure 2.2 Nozzle and skimmer inside the source chamber.

The gas mixture is produced inside a glass tube filled with cotton, soaked with the molecule (both CH_2Br_2 and $CHBr_3$ are in liquid form at room temperature). The input of the glass tube is connected to a He tank, while the output is linked to the nozzle.

By seeding the molecule under study to an unreactive carrier noble gas, in our case He, the molecule loses most of its internal energy due to frequent collisions with the gas atoms. Consequently, a cold molecular beam is produced through adiabatic expansion within the zone of silence.

2.3 Detection chamber

The second vacuum chamber of the VMI apparatus is called the detection chamber, and it serves as the location where the interaction between the laser and the molecular beam occurs, and where the resulting ions are subsequently detected. This chamber is maintained at a pressure of~10^{-7}mbar, achieved by utilizing a turbo-molecular pump (Pfeiffer HiPace700, 655lt/sec). Backing the turbo pump is a rotary oil mechanical pump (Leybold Trivac D25B, 25m³/h), which provides a backing pressure of ~$4x10^{-3}$Torr.

The detection chamber is divided into two regions by a gate valve: the interaction region and the Time of Flight (TOF) region. The interaction region incorporates the electrostatic optics of the single field setup introduced by Papadakis *et al.*[22]. It consists of a repeller and a grounded extractor that create an inhomogeneous lens-like field. A UV Fused Silica window with a Ø=40mm allows the laser beam to enter the chamber between the two electrostatic optics, perpendicular to the molecular beam. The beam is focused between the repeller-extractor setup using a converging lens with a focal length of 20cm.
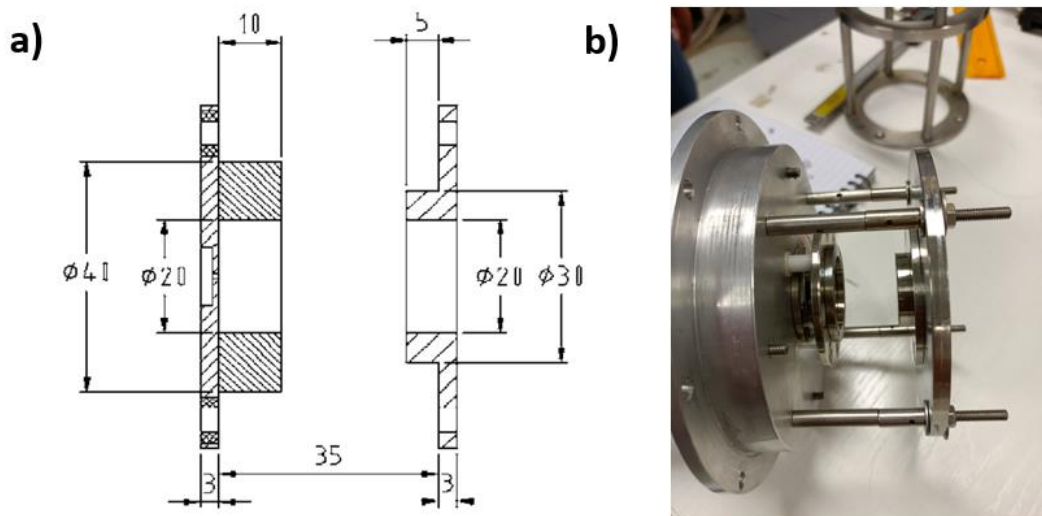

Figure 2.3 Electrostatic optics configuration of the VMI apparatus. In figure **a)** the dimensions of the repeller (left electrode) and the extractor (right electrode) are depicted in millimeters, idealized for a TOF region length of ~45cm (sourced from reference [22]. Figure **b)** is a photograph of the actual electrostatic setup.

The nascent photofragment ions are then accelerated by the electric field generated by the electrostatic optics and enter the ~45cm field-free TOF region. In this region, the ions are separated

based on their different mass-to-charge ratios and reach the position-sensitive detector at different times.

2.4 Laser beam

The laser beam employed for the photodissociation and photoionization of the molecules is generated by frequency doubling of the output of an excimer-pumped (Lambda Physic LPX, operating with XeCl at 308nm) pulsed dye laser (LPD3000, operating with Coumarin 102[25]), using a BBO crystal. The laser system functions at a repetition rate of 10Hz. The polarization of the beam is linear and aligns with the direction shown in Figure 2.1 **a)**. Also, the pulsed dye laser is shown in the Figure below.
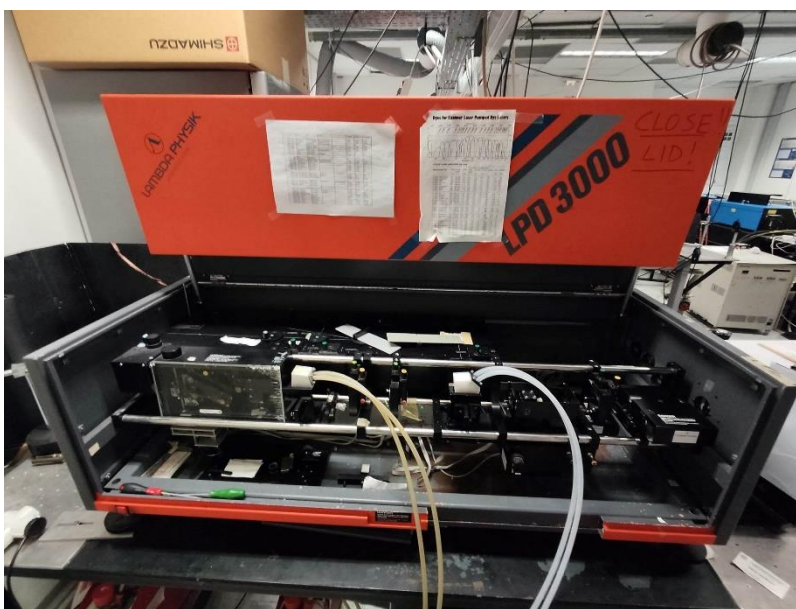

Figure 2.4 LPD 3000 pulsed dye laser.

2.5 Position-Sensitive Detector

The homebuilt Position-Sensitive Detector (PSD) is comprised of two Micro-Channel Plates (MCPs, BASPIK, $\emptyset$=50cm, Channel diameter=12μm), the MCP gate and the MCP back, coupled to a phosphor anode plate (Proxitronix, P47, $\emptyset$ = 40mm) and a CMOS Camera (Unibrain i702b).

Each MCP is comprised of small tubes (channels) arranged side by side with the same orientation. When an electric voltage is applied to MCP, it acts as an electron multiplier. Both MCPs and the phosphor plate are located at the end of the TOF region of the detection chamber.

During the molecular beam-laser interaction, when a nascent ion strikes the charged MCP, it emits a single electron per channel. These emitted electrons then undergo reflection within the inner surface of the channels, triggering an avalanche effect that generates many emitting electrons. The MCP Gate and MCP Back together provide an electron amplification of $\sim 10^6$ output electrons from a single input electron.
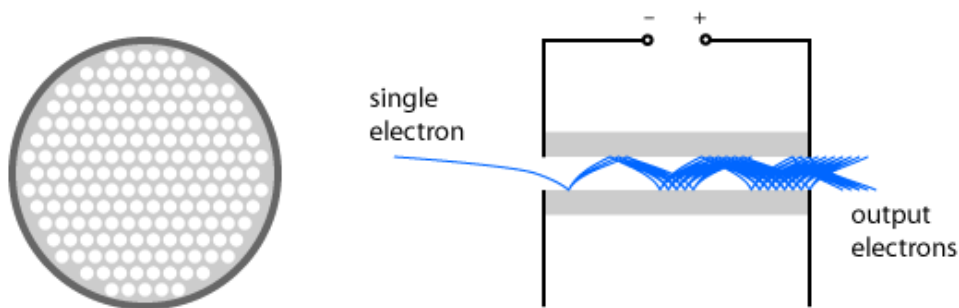

Figure 2.5 MCP and its operating principle.

The output electrons subsequently excite the phosphor plate, causing it to emit photons. Since the MCPs and phosphor are parallel to each other, the position where the ion strikes the PSD corresponds to the spot of photon emission The CMOS camera captures the emitted light from the phosphor, effectively recording an image that corresponds to the impact of the ion.

The PSD setup captures a frame of the detected ions approximately every second, corresponding to 10 laser and molecular beam pulses. Each frame represents the position and intensity of the ions (spatial distribution) at a specific moment in time. These frames are then saved and processed using a frame grabber program installed on the computer. The program averages a total of 400 frames to create an ion image, combining the information from multiple instances to enhance the signal-to-noise ratio.

During the data acquisition process, 10 ion images are recorded, capturing the ion distribution over time. Additionally, 5 background images are obtained with the nozzle off. These background images account for the signal detected by the PSD that does not originate from the molecular beam. Finally, the eventual image is obtained by summing the 10 averaged ion images and subtracting the 5 background images. The final image files are grayscale 16bit (RAW 1040x1040 pixels).

2.6 Detection modes

The PSD has two modes of operation. These are the continuous mode and the gated mode.

In continuous mode, the detector always remains on, allowing the detection of all the nascent ions from the molecular beam-laser reaction. The ion signal, known as the TOF mass spectrum, can be observed on an oscilloscope (Hameg HM1007), as shown in Figure 2.6. In this mode, the oscilloscope and the live video from the detector are used to optimize various setup parameters. These parameters include the relative time delay between the molecular beam and the laser pulse, the position of the converging lens that focuses the laser beam, and the laser beam's power. By fine-tuning these parameters, we aim to achieve the best possible ion signal. The voltages applied to the electronics in this mode are as follows: 1.6kV to the MCP back with the MCP gate grounded, 6kV to the phosphor, and 3-5kV to the repeller. Increasing the voltage applied to the repeller results in the detection of a wider range of ion kinetic energies. Reversing the voltage of the repeller allows for the focusing of nascent photoelectrons generated from the reaction, enabling the recording of images of the photoelectron distribution.

In gated mode, we can obtain the ion distribution of a specific photofragment by applying a pulse voltage to the MCP Gate. This voltage is applied at a precise time corresponding to the TOF of the desired ion (mass-to-charge ratio) and lasts for only tenths of nanoseconds. It is important to note that gated mode is primarily useful for cations detection since the photoelectrons produced from the ionization of all fragments have the same mass-to-charge ratio, resulting in the same time of flight. In this mode, the voltages applied to the electronics are as follows: 1.2kV to the MCP back, 6kV to the phosphor, a pulse voltage of -0.7kV to the MCP gate, and 3-5kV to the repeller.

2.7 Pulse generator

The VMI setup incorporates a pulse generator (Berkley Nucleonics, model BNC 565) to facilitate precise timing control. The pulse generator produces TTL pulses, with a repetition rate of 10Hz. These pulsed drive/trigger the voltage modulators of the piezoelectric nozzle, the MCP Gate, and the laser's external trigger input.

Each channel output of the pulse generator can be delayed with respect to the others with a user-specified time delay. This configuration allows for flexible timing arrangements within the setup.

Also, by using the pulse generator, it becomes possible to optimize the relative time delay between the molecular beam and the laser pulse. Additionally, it enables the selection of a specific time that the PSD works on gated mode, corresponding to the TOF of the desired ion. The pulse generator as well as the oscilloscope utilized are featured in Figure 2.6.
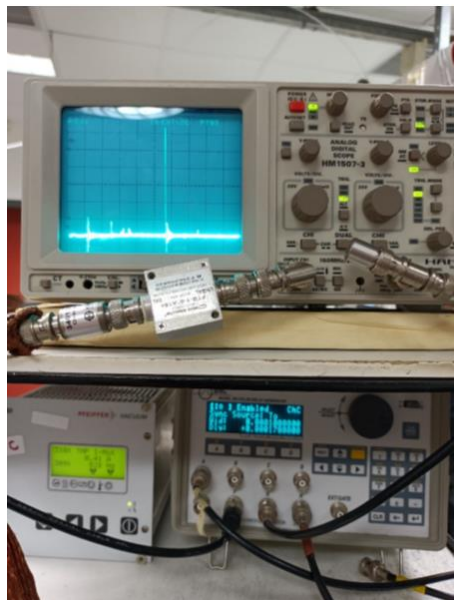

Figure 2.6 oscilloscope and pulse generator.

2.8 Image analysis

To extract the graph depicting the intensity versus kinetic energy release (KER distribution) of the detected ion photofragment, a series of analysis steps are implemented on the raw image files. The following steps outline the process:

1. First, we identify the specific pixel coordinates on the horizontal and vertical axes that correspond to the center of the image.
2. Next, a quadrat-weight averaging is applied to the raw file, considering a specified radius from the image's center. This process involves averaging pixel intensities within the designated radius while subtracting background noise originating outside of this region.
3. Then, the inverse Abel transform is applied to the image. This transform extracts the central slice of the 3D ion distribution from the 2D projection captured by the PSD. Before

applying the inverse Abel transform, it is essential to perform the second step, due to the transform's sensitivity to the image asymmetry and intensity variations.

4. Finally, after obtaining the reconstructed image through the previous steps, integration is performed by angle. This integration involves summing the intensities of all pixels within a given radius. By calibrating the detector using a procedure detailed in the following chapters, the resulting graph displays the intensity of the ions detected as a function of the KER.

The figure below depicts the images of CH_2^+ fragments originated by the photodissociation of CH_2Br_2 at 242nm and the reconstructed images by processes 2 and 3. The coloring of the images was applied using Adobe Photoshop CS6.
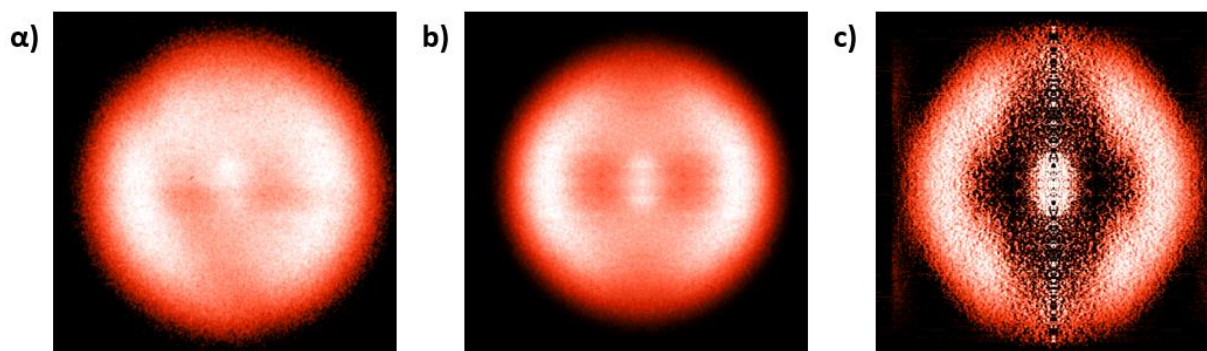

Figure 2.7 **a)** RAW image of the CH_2^+ fragments produced by the photodissociation of CH_2Br_2 at 242 nm. **b)** image reconstructed by process 2, **c)** image reconstructed by process 3

Chapter 3 Photodissociation of CH₂Br₂ at 242nm

3.1 Introduction

Dibromomethane, also known as methylene dibromide, is an organobromide compound with the chemical formula CH_2Br_2. The central carbon atom in dibromomethane exhibits sp^3 hybridization, resulting in a tetrahedral molecular geometry. Furthermore, dibromomethane possesses C_{2v} symmetry, characterized by a two-fold axis of symmetry and two perpendicular mirror planes that intersect along the principal axis. The figure below depicts the structural formula of dibromomethane:
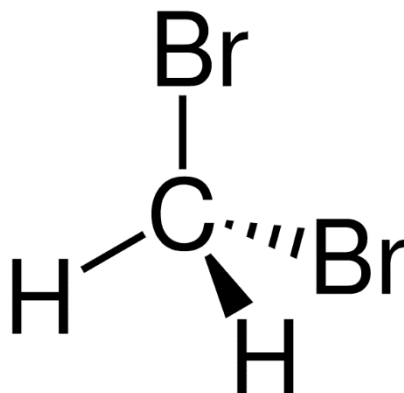

Figure 3.1 Dibromomethane structural formula. Sourced from Wikipedia (https://en.wikipedia.org/wiki/Dibromomethane).

Dibromomethane is a colorless liquid, at room temperature, with a pleasant odor that is commonly used as a solvent and motor fuel[26]. It has a density of 2.477 g/cm^3, making it denser than water. Also, dibromomethane is not soluble in water. It is naturally produced by marine algae[27,28], and it can also be synthesized in the laboratory.

The UV-Vis photochemistry of dibromomethane, along with other bromine-containing compounds, has been the subject of extensive scientific research over the past three decades. This is because reactive bromine and the radicals formed through the photodissociation of these compounds are known to contribute to stratospheric ozone depletion[29], both directly and catalytically. Dibromomethane is a significant bromine-containing substance that plays a role in ozone depletion, as it is responsible for releasing approximately 20% of the total atmospheric bromine in the upper atmosphere [30,31].

Furthermore, the influence of the reactive bromine atoms produced by such compounds has received considerably less attention compared to the chloride atoms produced by chlorine-containing compounds like the well-known chlorofluorocarbons (CFCs). Despite bromine's lower concentration in the atmosphere compared to chloride, it is significantly more destructive on an atom-for-atom basis. Studies suggest that bromine may be as much as 100 times more destructive than chlorine[32]. This emphasizes the significance of studying the photochemistry of bromine-containing molecules, such as dibromomethane.

Huang *et al.*[33] studied the photodissociation dynamics of the ion $CH_2Br_2^+$ by means of VMI and TOF mass spectroscopy at 355nm. Their results revealed the production of highly vibrationally excited CH_2Br^+ fragments and a branching ratio of Br in the spin-orbit excited state, $Br^*(^2P_{1/2})$, to Br in the ground state, $Br(^2P_{3/2})$ as 2.2:1. Furthermore, ab initio calculations supported the internal mechanism driving the dissociation process.

Sharma *et al.*[34] performed experimental and theoretical studies on the 355 nm laser-induced dissociation/ionization of CH_2Br_2 using a TOF mass spectrometer. The energetics of different dissociation channels in the ground state of CH_2Br^+/CH_2Br was investigated through ab initio calculations, suggesting a mechanism involving the dissociation of CH_2Br_2 into CH_2Br, followed by ionization of the resulting products.

Lee *et al.*[35] studied the photodissociation of CH_2Br_2 at 248 nm, revealing that it undergoes simple C-Br bond fission with anisotropic recoil of fragments. As the laser energy increased, the nascent products CH_2Br absorbed an additional photon to detach a secondary Br atom.

Ji *et al.*[36] investigated the photodissociation dynamics of CH_2Br_2 at 234 and 267 nm using the VMI technique coupled with a REMPI scheme. The results showed that the translational energy distributions of Br and Br* atoms consisted of two components related to the radical channel and secondary dissociation process. The findings suggested a non-adiabatic coupling between electronic states and revealed that fragments predominantly recoiled along the Br-Br direction during the photodissociation process.

Long *et al.*[37] recorded and analyzed the (2 + n) REMPI spectra of CH_2Br_2 in the two-photon resonance excitation region from 71,200 to 82,300 cm^{-1}. The spectra allowed the characterization of new molecular Rydberg states, identification of the $C^*(^1D_2)$ intermediate in the

photodissociation processes and provided insights into the electronic states of CH. Furthermore, the observed bromine atomic resonances at specific wavenumbers were associated with bromine atom formation via predissociation of CH_2Br_2 Rydberg states, solving long-standing puzzles regarding CH spectroscopy and energetics.

In this study, we investigated the photodissociation dynamics of CH_2Br_2 by means of VMI at 242nm. Our investigation comprised capturing images of the nascent ion photofragments and photoelectrons. By analyzing these images, we obtained graphs representing the intensity of the detected ions and photoelectrons in relation to their KER. Through the analysis of these graphs, we identified the active photoexcitation and photodissociation pathways, as well as calculated the internal energy of the products and reactants involved in each photodissociation reaction.

3.2 Experiment

For our experiments, we employed the apparatus introduced in detail in Chapter 2. The laser energy was maintained at ~1mJoule/pulse, with ~0.3mJoule/pulse entering the source chamber.

We captured images of the photoelectrons generated by the photodissociation process using PSD in continuous mode. The repeller's voltage was set to -4kV, causing electrons to be repelled towards the PSD while ions were pushed away. By utilizing the image analysis explained in Chapter 2 we acquire a graph illustrating the intensity of photoelectrons relative to their KER was produced. From the peaks in the graph, we were able to determine the specific neutral fragments produced during the photodissociation process. These fragments were subsequently ionized by the laser beam, allowing us to detect their nascent photoelectrons. The values of ionization potentials (IP) of the neutral photofragments were obtained from the NIST Chemistry WebBook[11].

Next, we switched the PSD to gated mode and adjusted the repeller's voltage to +4kV to capture images of the nascent ion fragments. Following image analysis, we obtained graphs showing the intensity of each ion fragment relative to its KER (KER distributions). Each ion was detected as having KER within a specific range. We used the KER data, as well as equations 1.1 and 1.20, to identify, from all possible pathways, those most likely to produce the observed KERs.

The bond dissociation energy values (D_0) required, although not found in the literature, were calculated using the enthalpies of formation for the dissociating compound and the nascent

fragments. The enthalpy of formation (ΔH_f) is the change in enthalpy that occurs when one mole of a compound is formed from its constituent elements in their standard states at a specified temperature and pressure. The calculation of D_0 were performed using the following formula:

$$D_0(R - X) = \Delta H_f(R) + \Delta H_f(X) - \Delta H_f(RX) \qquad 3.1$$

Here, $D_0(R\text{-}X)$ is the D_0 needed to break the bond between the radical R (the remaining part of the compound) and the atom X. The enthalpies of formation (ΔH_f) used in the calculation were obtained from Burcat's database[38] and correspond to the enthalpies of formation at 0K.

Furthermore, the D_0 of the ion compounds were calculated by the D_0 values of their corresponding neutral compounds, along with the IP values, by following the logic depicted in Figure 3.2.
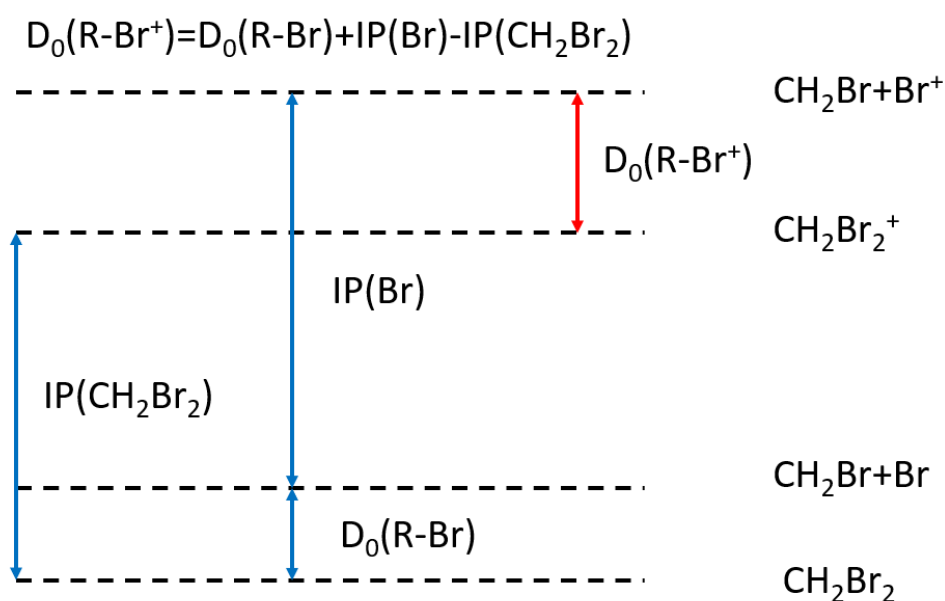
Figure 3.2 Calculation of $D_0(R\text{-}Br^+)$ of CH_2Br_2.

3.3 Results and Discussion

3.3.1 Calibration of KERs

As explained in Chapter 2, process 4 of the image analysis technique is utilized to create the graph corresponding to the intensity of the detected ions (or photoelectrons) as a function of the radius from the image center in pixels. The kinetic energy of the detected ion follows a proportional relationship with the square of the radius, as represented by the equation:

$$KER = A(pixels)^2 \qquad\qquad 3.2$$

Because of the use of lens-like electrodes in VMI, the proportionality factor A needs to be determined. This is succeeded by employing a well-studied photodissociation reaction.

During the calibration process for photoelectron detection using the PSD, while applying a voltage of -4kV to the repeller, we recorded the image of photoelectrons while the laser's wavelength was adjusted for a (2+1) REMPI scheme targeting H atoms. The intermediate state chosen for excitation was the first excited electronic state[39] $^2P_{1/2}$. To excite H atoms from their ground state to the intermediate $^2P_{1/2}$ state, each of the two required photons must have an energy of approximately 5.099 eV, corresponding to a wavelength of 243.135 nm. Through the calibration process, we determined the wavelength offset between the laser's control setting and the actual wavelength used. This offset was approximately 0.276 nm, resulting in the real wavelength utilized for studying the photodissociation dynamics of CH_2Br_2 and $CHBr_3$ being 242.276 nm, equivalent to a photon energy of 5.117 eV.

The figure below displays the recorded photoelectrons' image captured by the PSD after undergoing image analysis steps 1-3, along with the corresponding graph depicting intensity as a function of the radius in pixels. The peak with the highest intensity corresponds to the photoelectrons produced by the (2+1) REMPI process targeting hydrogen, as expected due to the state-selective nature of the scheme. The KER of the photoelectrons resulting from the REMPI of H is calculated using equations 1.1 and 1.20 to be 1.699 eV, which provides us with the calibration factor value: $A = 3.928 * 10^{-5}$ eV/px^2.
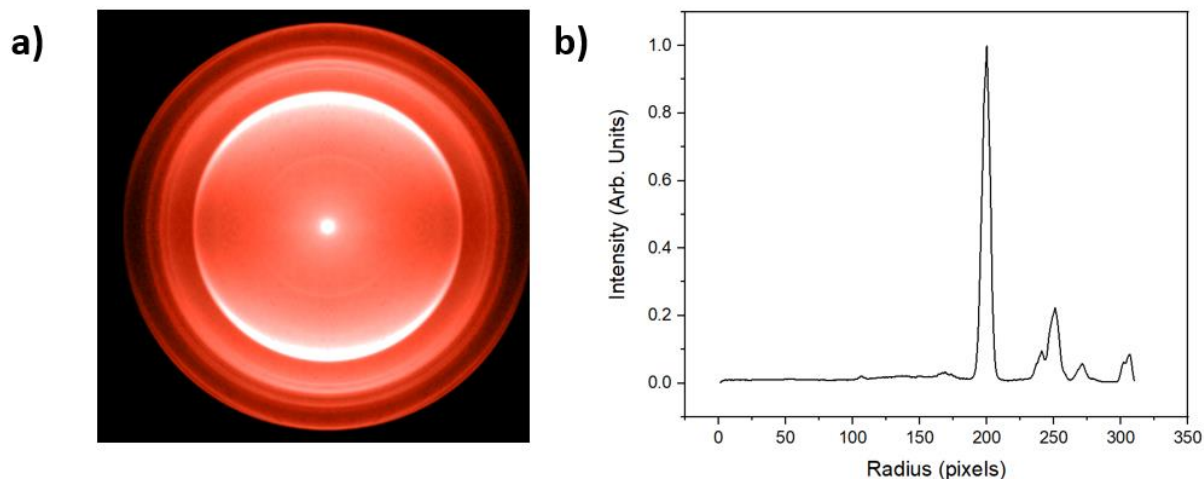
Figure 3.4 **a)** Recorded image of photoelectrons while employing (2+1) REMPI scheme targeting H atoms. **b)** Graph of intensity as a function of radius reconstructed from the photoelectrons' image. The peak with the highest intensity corresponds to the KER of photoelectrons produced by the ionization of the H atoms at $^2P_{1/2}$ excited state.

Similarly, we calculate the calibration factor of the PSD while detecting the I^+ fragments generated from the photodissociation of CH3I at a wavelength of 242.276nm and applying a voltage of +4kV to the repeller.
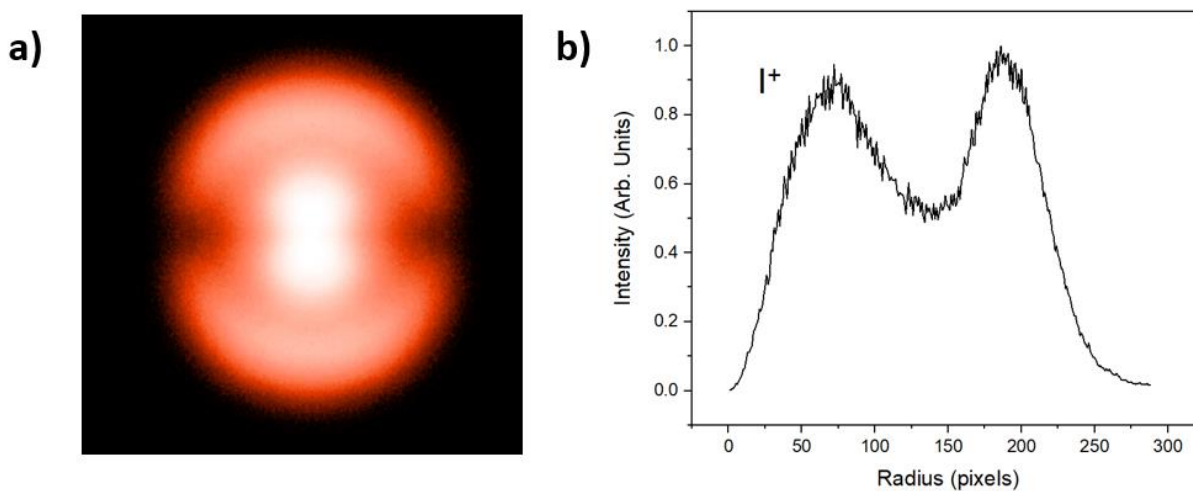
Figure 3.3 **a)** Recorded image of I^+ produced by the photodissociation of CH_3I at 242.276nm. **b)** Graph of intensity as a function of radius reconstructed from the I^+ image.

In the resulting graph, the first peak on the left corresponds to I in the first excited electronic state [39] $^2P_{1/2}$, while the second peak represents I in the ground state. From these peaks, we obtained the calibration factor, which has a value of $A=3.599*10^{-6}eV/px^2$.

3.3.2 Photoelectrons

Figure 3.5 depicts the recorded image of photoelectrons produced by the photodissociation of CH_2Br_2 as well as the KER distribution graph.
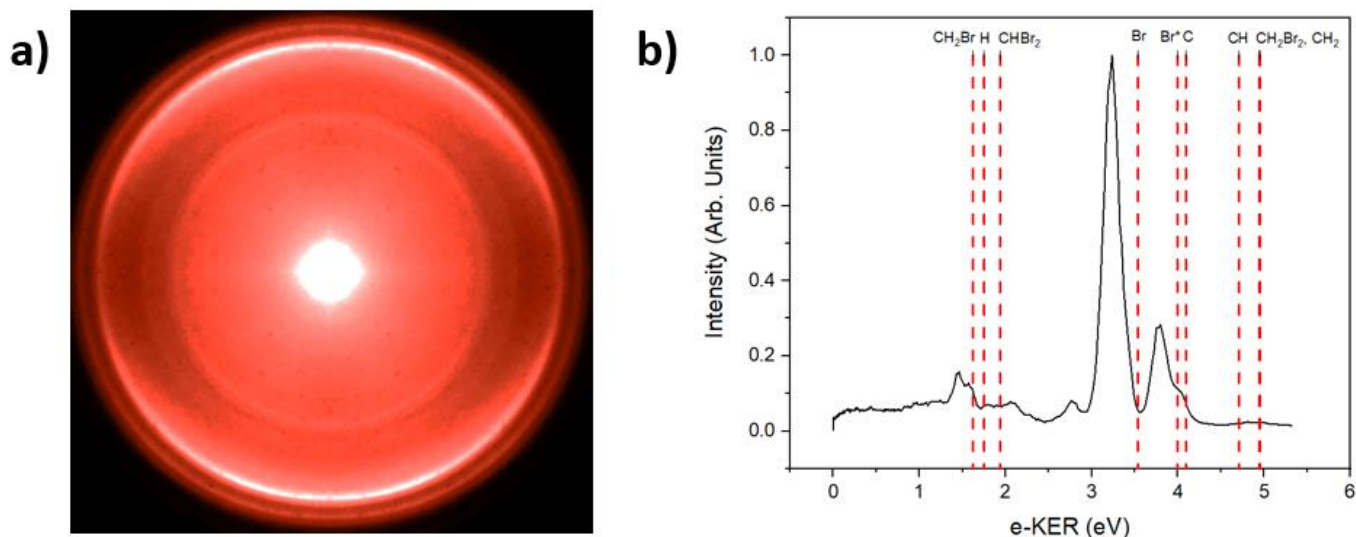

Figure 3.5 **a)** Recorded image of photoelectrons produced by the photodissociation of CH_2Br_2. **b)** Graph of photoelectrons' intensity as a function of KER along with the designated peaks.

The photoelectrons' image shows 9 rings corresponding to photoelectrons produced by the ionization of 9 different neutral compounds. The designation of the peaks was determined by calculating the photoelectron kinetic energy release (KER) for the photoionization of all possible neutral fragments and comparing them to the observed KER corresponding to the rings in the recorded image. The compounds associated with each ring are as follows:1) CH_2Br (1.625eV), 2) H (1.753eV), 3) $CHBr_2$ (1.935eV), 4) Br (ground state, 3.538eV), 5) Br* (first excited state $^2P_{1/2}$, 3.995eV), 6) C (4.092eV), 7) CH (4.712eV), 8) CH_2Br_2(parent molecule, 4.942eV) and 9) CH_2 (4.956eV).

All compounds require 3 photons to get ionized, except for $CHBr_2$ and CH_2Br which require 2.

3.3.3 Ions

Figure 3.6 depicts the recorded images of ions produced by the CH_2Br_2-laser interaction.
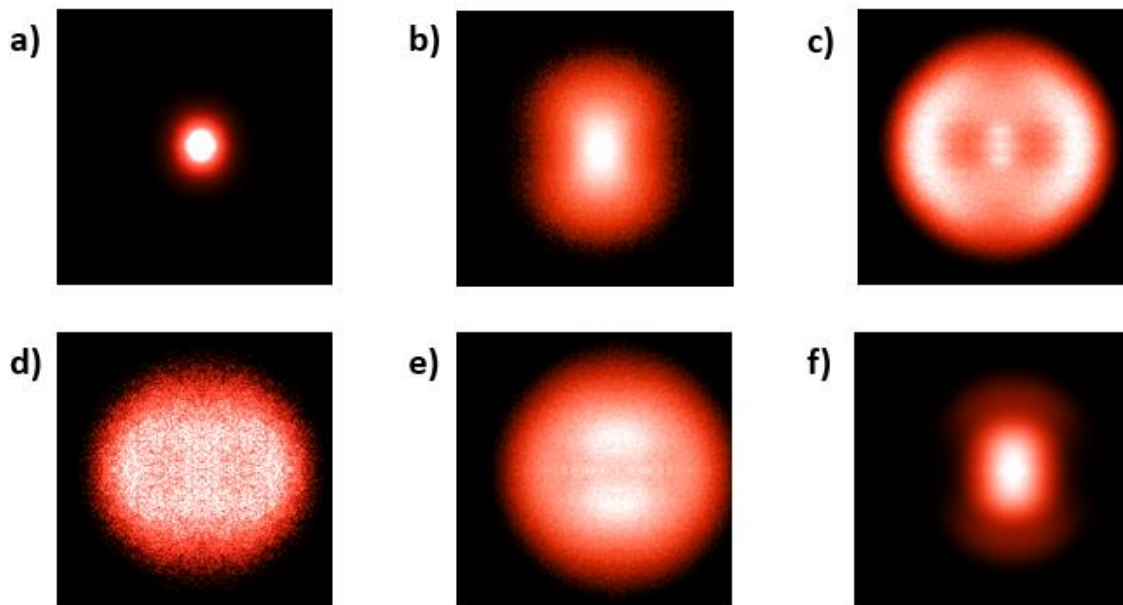

Figure 3.7 Recorded images of ions produced by the CH_2Br_2-laser interaction. **a)** $CH_2Br_2^+$, **b)** CH_2Br^+, **c)** CH_2^+, **d)** CH^+, **e)** C^+, **f)** Br^+

From these images, we obtain the following KER distributions and determined the active photofragmentation pathways leading to the detected ions.
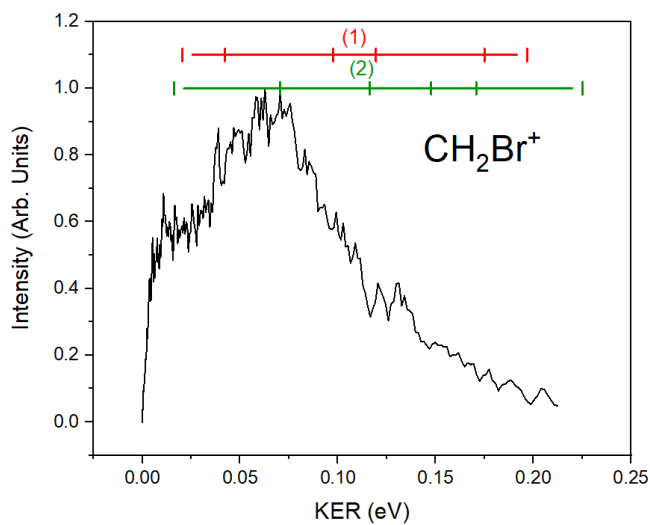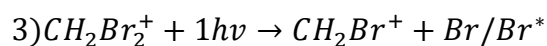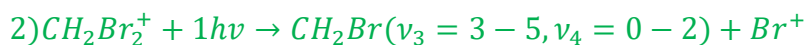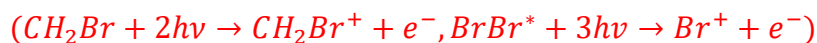

Figure 3.6 KER graph of CH_2Br^+.

The KER of the CH_2Br^+ was detected to be within the range of 0-0.21eV.

$$1) CH_2Br_2 + 1hv \rightarrow CH_2Br(v_3 = 9 - 14) + Br/Br^*$$

$$(CH_2Br + 2hv \rightarrow CH_2Br^+ + e^-, BrBr^* + 3hv \rightarrow Br^+ + e^-)$$

$$(CH_2Br_2 + 3hv \rightarrow CH_2Br_2^+ + e^-)$$

$$2) CH_2Br_2^+ + 1hv \rightarrow CH_2Br(v_3 = 3 - 5, v_4 = 0 - 2) + Br^+$$

$$3) CH_2Br_2^+ + 1hv \rightarrow CH_2Br^+ + Br/Br^*$$

Processes 1-3 are all the photodissociation reactions that yield CH_2Br/CH_2Br^+ radicals. Process 1 corresponds to the neutral parent molecule's photodissociation, while processes 2 and 3 correspond to the cation parent molecule's photodissociation, initially ionized by 3 photons, as noted above in reaction 2. These processes generate radicals in both neutral and ion forms. It is worth mentioning that, as indicated in process 1, the products are ionized by the laser beam before detection. This ionization step applies to all following photofragmentation processes and the resulting neutral products, therefore it doesn't need to be explicitly stated for each process.

In process 1, the internal energy of the CH_2Br must be within the range of 1.51-2.35eV, for the process to produce both CH_2Br and Br/Br^* between their detected KER ranges (Br^+ KER range is 0-0.28eV). If the assumption is made that it all comprises excitation to the vibrational mode v_3 (CH_2 scissor), it is achieved by excitation to energy levels n=9-14. Similar reasoning was applied to all the photodissociation processes to explain as much KER range of the detected radicals as possible.
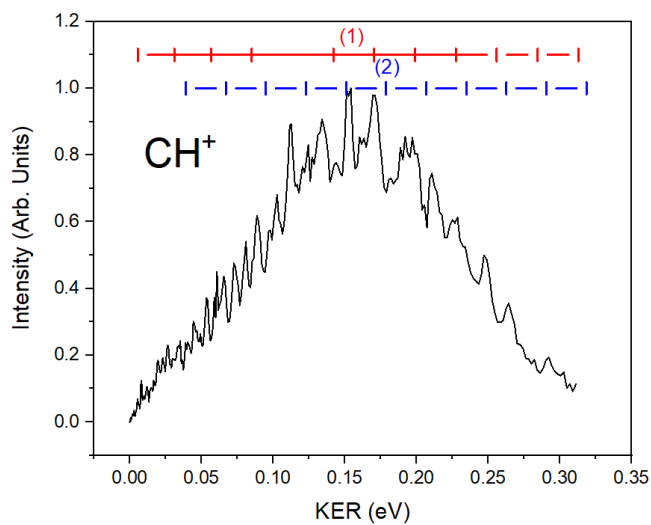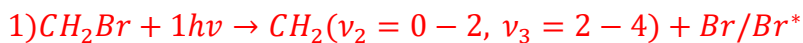
Several processes have been deemed not as active, based on the KER range of their corresponding products, the total number of photons required to obtain the detected radical, and whether the subsequent reactions following their products' dissociation result in more dissociation pathways.

As an example, process 3 was deemed inactive, since it produces CH_2Br^+ radicals with kinetic energy of 1.93eV and 1.73 eV for the Br and Br* reactions respectively, far exceeding their detected KER range. Similar tests were performed for all possible photodissociation reactions leading to all the detected radicals.
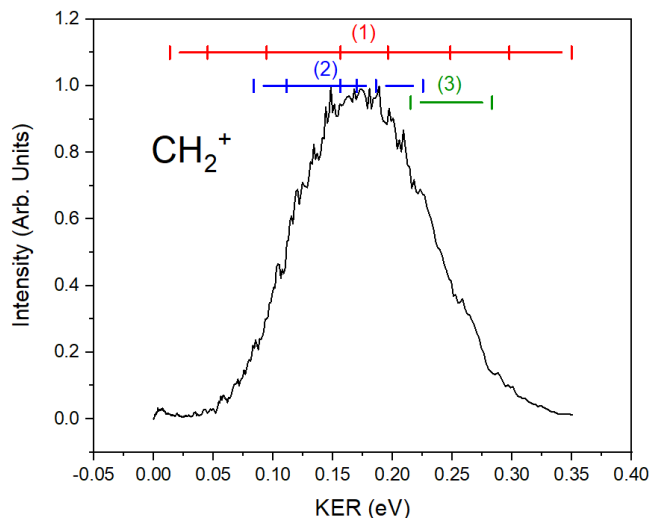
Figure 3.8 KER graph of CH$_2$$^+$.

 The KER of the CH$_2$$^+$ was detected to be within the range of 0-0.35eV.

All the following photodissociation reactions yielding CH$_2$/CH$_2$$^+$ fragments were deemed active. Process 1 yields vibrationally excited CH$_2$, whereas the subsequent reactions necessitate internally excited CH$_2$Br$^+$ to occur with a single photon.

$$1) CH_2Br + 1hv \rightarrow CH_2(v_2 = 0 - 2, v_3 = 2 - 4) + Br/Br^*$$

$$2) CH_2Br^+(v_1 = 1,2, v_4 = 0,1) + 1hv \rightarrow CH_2^+ + Br/Br^*$$

$$3) CH_2Br^+(v_1 = 5 \ or \ v_5 = 5) + 1hv \rightarrow CH_2 + Br^+$$

Figure 3.9 KER graph of CH$^+$.

The KER of the CH^+ was detected to be within the range of 0-0.31eV.

$$1) CH_2(v_3 = 0 - 9) + 1hv \rightarrow CH(v = 0 - 2) + H$$

$$2) CH_2^+(v_3 = 0 - 9) + 1hv \rightarrow CH^+(v = 0 - 2) + H$$

The photodissociation process $CH_2^+ \rightarrow CH + H^+$ requires 2 photons to occur, and consequently is considered less active. Nevertheless, both CH_2 and CH_2^+ produced by the previous processes dissociate to produce subsequent fragments.
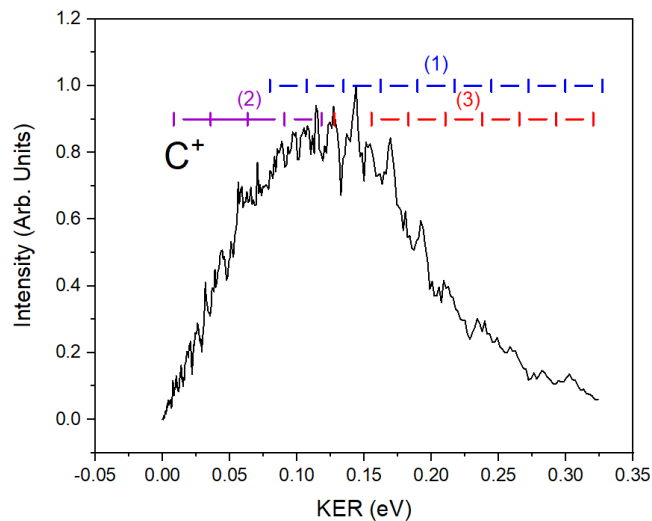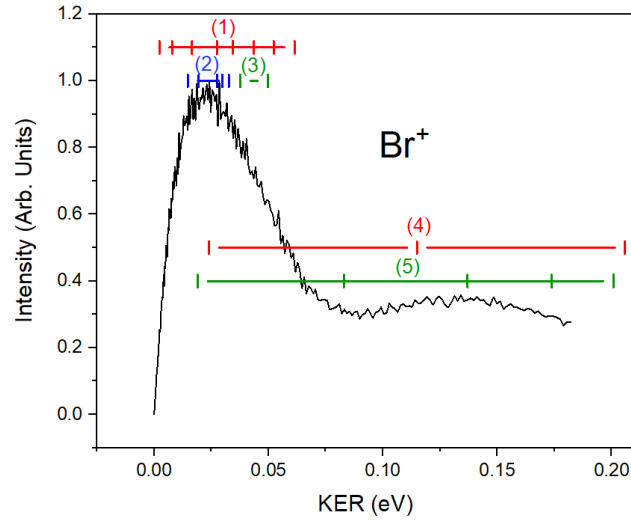

Figure 3.10 KER graph of C⁺.

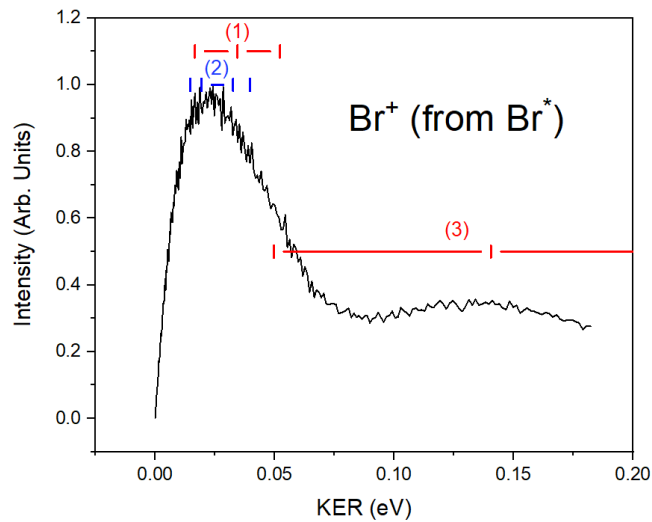The KER of the C⁺ was detected to be within the range of 0-0.32eV.

All possible photodissociation reactions yielding C/C⁺ fragments were deemed active. These are:
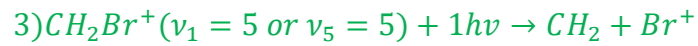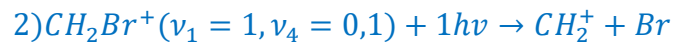
$$1) CH^+(v = 0 - 9) + 1hv \rightarrow C^+ + H$$

$$2) CH^+(v = 4 - 9) + 1hv \rightarrow C + H^+$$

$$3) CH(v = 0 - 7) + 1hv \rightarrow C + H$$

Comments have already been provided for the processes listed below, which are associated with the production of Br, Br*, and Br⁺ within the observed KER range.

Figure 3.12 KER graph of Br⁺.

The KER of the Br^+ was detected to be within the range of 0-0.23eV.

$$1) CH_2Br + 1hv \rightarrow CH_2(v_2 = 0-2, v_3 = 3,4) + Br$$

$$2) CH_2Br^+(v_1 = 1, v_4 = 0,1) + 1hv \rightarrow CH_2^+ + Br$$

$$3) CH_2Br^+(v_1 = 5 \ or \ v_5 = 5) + 1hv \rightarrow CH_2 + Br^+$$

$$4) CH_2Br_2 + 1hv \rightarrow CH_2Br(v_3 = 12 - 14) + Br$$

$$5) CH_2Br_2^+ + 1hv \rightarrow CH_2Br(v_3 = 3 - 5, v_4 = 0 - 2) + Br^+$$

Figure 3.11 KER graph of Br⁺ produced by the ionization of Br*.

$$1) CH_2Br + 1hv \rightarrow CH_2(v_2 = 0 - 2, v_3 = 2) + Br^*$$

$$2)CH_2Br^+(v_1 = 2, v_4 = 0,1) + +1hv \rightarrow CH_2^+ + Br^*$$

$$3)CH_2Br_2 + 1hv \rightarrow CH_2Br(v_3 = 9 - 11) + Br^+$$

3.4 Conclusions

The summary of all the active photodissociation reactions is depicted in Figure 3.13.
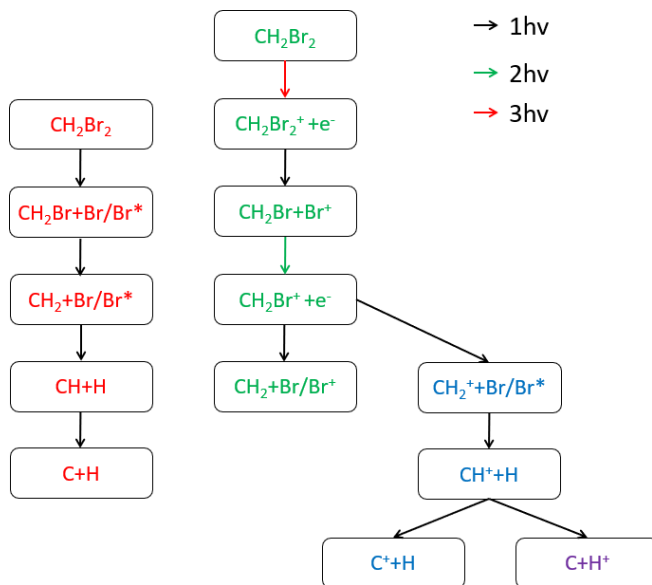

Figure 3.13 Photodissociation pathways' diagram

The photodissociation pathway on the left (red color) corresponds to the photofragmentation of the neutral parent molecule, while the photodissociation pathway on the right corresponds to the photofragmentation of the cation parent molecule. These channels effectively account for the entire observed KER range of the detected ion fragments, while also demonstrating that the photodissociation radicals are generated with high internal energy excitations.

Furthermore, the results obtained from the ion images are consistent with those obtained from the photoelectron images. We successfully acquired both ion images and photoelectrons for most compounds, except for H and $CHBr_2$, where we only detected the photoelectrons. Nevertheless, the photodissociation reactions of the subsequent fragments of $CHBr_2$ are included in the photodissociation pathways' diagram, with their products associated with other fragments of the parent molecule.

Moreover, during the photodissociation process, H^+ atoms absorb a significant portion of the total KER due to their lower mass. Consequently, we were not able to detect their KER distribution since their energies surpass the range of the detector.

Chapter 4 Photodissociation of CHBr₃ at 242nm

4.1 Introduction

Bromoform, also known as tribromomethane, is a brominated organic solvent with the chemical formula $CHBr_3$. The central carbon atom in bromoform exhibits sp^3 hybridization, resulting in a tetrahedral molecular geometry. Furthermore, bromoform possesses C_{3v} symmetry, characterized by a three-fold axis of symmetry and three perpendicular mirror planes that intersect along the principal axis. The figure below depicts the structural formula of bromoform.
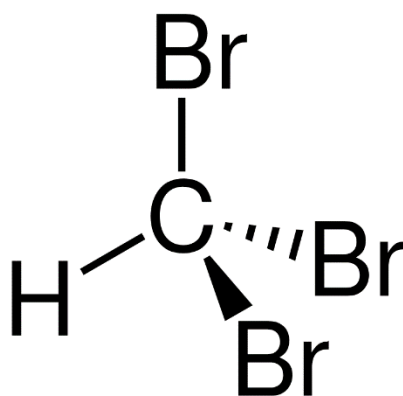

Figure 4.1 Bromoform structural formula. Sourced from
Wikipedia (https://en.wikipedia.org/wiki/Bromoform).

Bromoform is a light-yellow liquid with a sweet odor reminiscent of chloroform. It was previously employed as a solvent, flame retardant, and sedative. Nowadays, its primary application is as a reagent, particularly as an extraction solvent. With a density of 2.9 g/cm³, bromoform is denser than water. Also, it is slightly soluble in water[40].

Naturally, bromoform can be found in the oceanographic and biogeochemical regime of the subtropical Northeast Atlantic, where it is produced by algae and kelp as a byproduct of the photosynthetic process[27]. Additionally, it can be synthesized in the laboratory.

The significance of studying the UV-Vis photochemistry of bromine-containing molecules has already been established in Chapter 3. Bromoform is one of several organobromide compounds that contribute active bromine atoms to the atmosphere. Moreover, of all the bromomethane derivatives, bromoform has been found to be the greatest contributor of bromine to the Artic atmosphere[41].

McGivern et al.[42] studied the photodissociation of CHBr$_3$ at 193 nm using the photofragment translational spectroscopy technique and provided a detailed analysis of the primary and secondary dissociation channels. The primary dissociation involves the loss of a bromine atom, while a fraction of the resulting CHBr$_2$ radicals undergo secondary dissociation via the elimination of both HBr and Br with comparable yields. The experimental findings are supported by ab initio calculations and RRKM estimates.

Xu et al.[43] studied the photodissociation of bromoform at 234 and 267 nm using TOF mass spectrometry and VMI. The findings reveal the formation of ground and excited state Br atoms, as well as Br$_2$ through a primary elimination channel. These findings challenge existing atmospheric models by indicating that CHBr$_3$ photodissociation releases both Br atoms and Br$_2$, suggesting a need to reevaluate their implications for atmospheric bromine chemistry.

Huang et al.[44] investigated the photodissociation dynamics of CHBr$_3^+$ at different wavelengths using TOF mass spectrometry and VMI. The results show that at 355 and 610 nm, only CHBr$_2^+$ ions are observed, indicating a single dissociation channel. At 308 nm, two additional channels involving molecular bromine elimination and three-body dissociation are observed. The experimental results provide insights into the energetics, dynamics, and dissociation pathways of CHBr$_3^+$.

Zou et al.[45] explored the photodissociation of CHBr$_3$ at 248 nm using VUV ionization photofragment translational spectroscopy. The dominant dissociation channel is the C-Br bond fission, and secondary photodissociation of CHBr$_2$ and CHBr leads to various product signals including Br, CHBr, CBr, HBr, and Br$_2$. Their study concludes that the C-Br bond breaking is the most significant photodissociation channel in the UV region, while the secondary channels involving HBr and Br$_2$ have minimal occurrence.

Tang et al.[46] studied the photodissociation dynamics of alkyl bromides, including CHBr$_3$, using REMPI along with TOF mass spectrometry. The branching ratios of Br and Br* were determined, revealing different dissociation channels. The REMPI spectrum of bromine atoms was also recorded, identifying 42 transition lines, with most matching with previous results. The study shows that bromine atoms produced from the photolysis of alkyl bromides primarily exist in the ground state.

Yang *et al.*[47] investigated the multiphoton photolysis reaction of bromomethanes, including $CHBr_3$, at 266 nm using nascent emission spectroscopy and laser-induced dispersed fluorescence spectroscopy. Excited species such as CH, Br, and C_2 are observed in the nascent emission spectra, and reaction intermediates like CHBr are identified. The study confirms a sequential atomic elimination mechanism, with C-Br bond dissociation being the most dominant.

In this study, we investigated the photodissociation dynamics of $CHBr_3$ by means of VMI at 242nm. Our study involved capturing images of the nascent ion photofragments and photoelectrons. By analyzing these images, we generated graphs illustrating the detected ions and photoelectrons' intensity relative to their KER. Through the analysis of these graphs, we identified the active photoexcitation and photodissociation pathways, as well as calculated the internal energy of the products and reactants involved in each photodissociation reaction.

4.2 Experiment

The conducted experiment followed a similar procedure to the study on the photodissociation dynamics of CH_2Br_2 at 242nm, described in Chapter 3. However, there were a few variations. The laser energy was kept at ~1.5 millijoules/ pulse, with ~ 0.5 millijoules/pulse entering the source chamber. Additionally, the voltage of the repeller was set at -5kV while the PSD, operating in continuous mode, was capturing images of the generated photoelectrons.

4.3 Results and Discussion

4.3.1 Calibration of KERs

The images of all the ion fragments were detected while the repeller's voltage was set to +4kV. Consequently, the calibration factor of the detector while detecting ions is the same as the one used in Chapter 3, which is: $A=3.599*10^{-6}eV/px^2$.

The images of the photoelectrons' produced by the molecular beam-laser interaction were recorded while the repeller's voltage was set at -5kV, thus a new calibration factor needed to be calculated.

To achieve the calculation of this new calibration factor, we recorded images of the photoelectrons produced by the interaction between the CH_2Br_2 molecule and the laser beam with its wavelength adjusted for a (2+1) REMPI scheme targeting the nascent Br* $(4s^24p^5 \ ^2P_{1/2})$ atoms. The

intermediate state chosen was the $4s^2 4p^4(^1D)5p\ ^2P_{1/2}$. The energy of each of the two photons required for the excitation of the Br atom from the first excited to this intermediate state is 5.196eV, corresponding to a wavelength of 238.624nm.

The figure below displays the recorded photoelectrons' image captured by the PSD after undergoing image analysis steps 1-3, along with the corresponding graph depicting intensity as a function of the radius in pixels. The peak with the highest intensity corresponds to the photoelectrons produced by the (2+1) REMPI process, as expected due to the state-selective nature of the scheme. The new calibration factor value is $A=4.936*10^{-5} eV/px^2$.
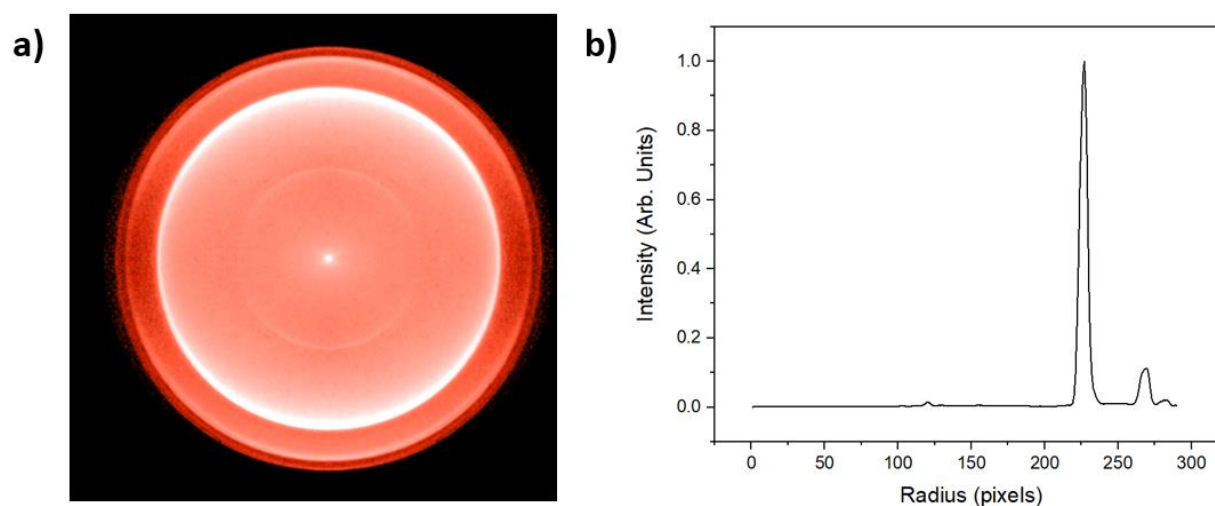

Figure 4.2 **a)** Recorded image of photoelectrons while employing (2+1) REMPI scheme targeting Br atoms at their first excited state. **b)** Graph of intensity as a function of radius reconstructed from the photoelectrons' image. The peak with the highest intensity corresponds to the KER of photoelectrons produced by the ionization of the Br* atoms at $^2P_{1/2}$ excited state.

4.3.2 Photoelectrons

Figure 4.3 depicts the recorded image of photoelectrons produced by the photodissociation and ionization process of $CHBr_3$, as well as the constructed graph of intensity as a function of KER.

The photoelectrons' image shows 7 rings corresponding to photoelectrons produced by the ionization of 7 different neutral compounds. The designation of the peaks was determined by calculating the photoelectron kinetic energy release (KER) for the photoionization of all possible neutral fragments and comparing them to the observed KER corresponding to the rings in the recorded image. The compounds associated with each ring are the following: 1) CBr_2 (0.125eV), 2) H (1.753eV), 3) $CHBr_2$ (1.935eV), 4) CBr_3 (2.735eV), 5) Br (ground state, 3.538eV), 6) Br* (first excited state, 3.995eV), 7) C (4.092eV).
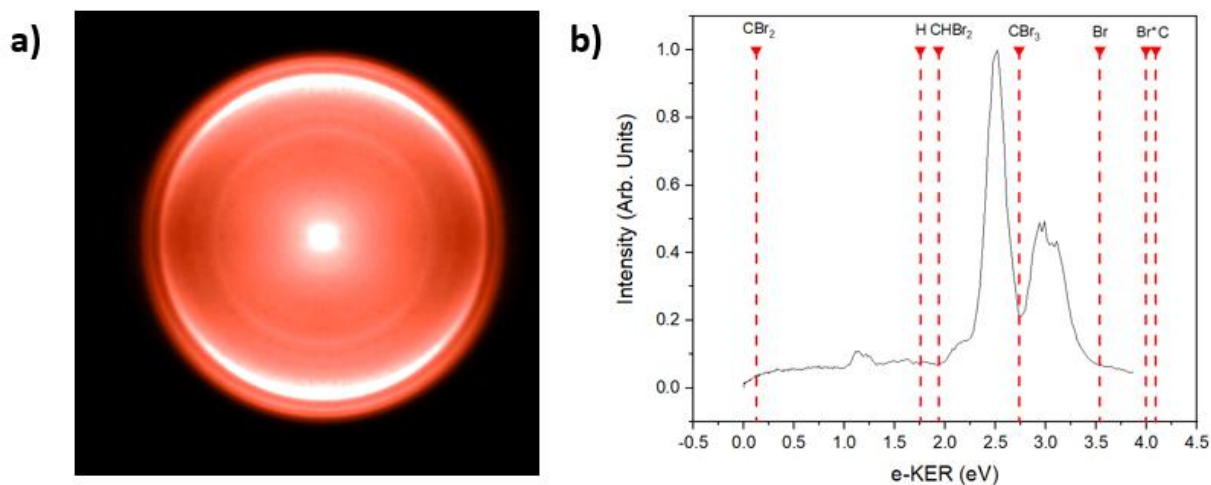
Figure 4.3 **a)** Recorded image of photoelectrons produced by the photodissociation of CHBr₃. **b)** Graph of photoelectrons' intensity as a function of KER along with the designated peaks.

The compounds CBr_2, $CHBr_2$, and CBr_3 require 2 photons to get ionized, while the rest require 3.

4.3.3 Ions

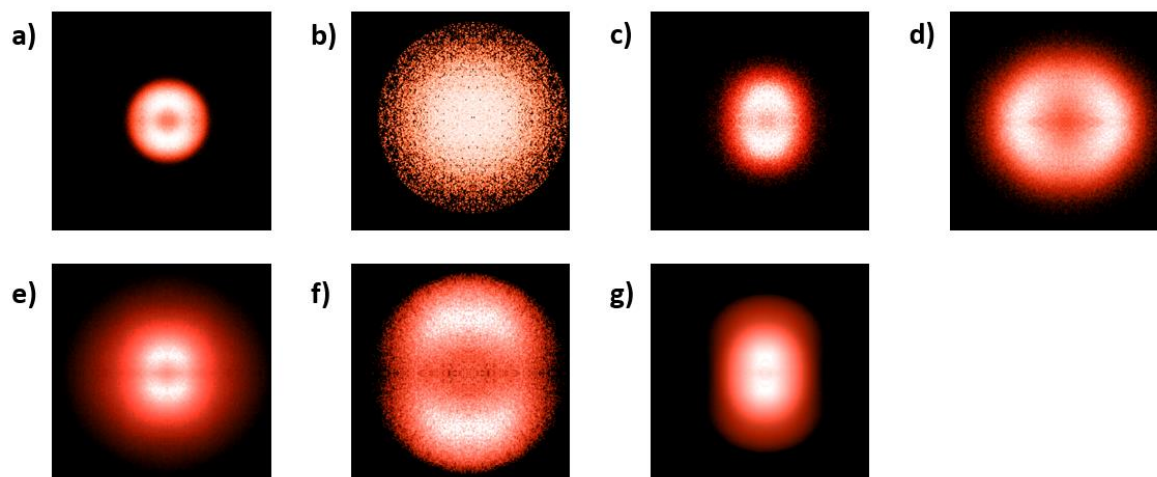Figure 4.4 depicts the recorded images of the ions produced by the CHBr₃-laser interaction.

Figure 4.4 Recorded images of ions produced by the CHBr₃-laser interaction. **a)** $CHBr_2^+$, **b)** $CHBr^+$, **c)** CBr^+, **d)** CH^+, **e)** C^+, **f)** H^+, **g)** Br^+.

From these images, we obtain the following KER distributions and determined the active photofragmentation pathways leading to the detected ions.
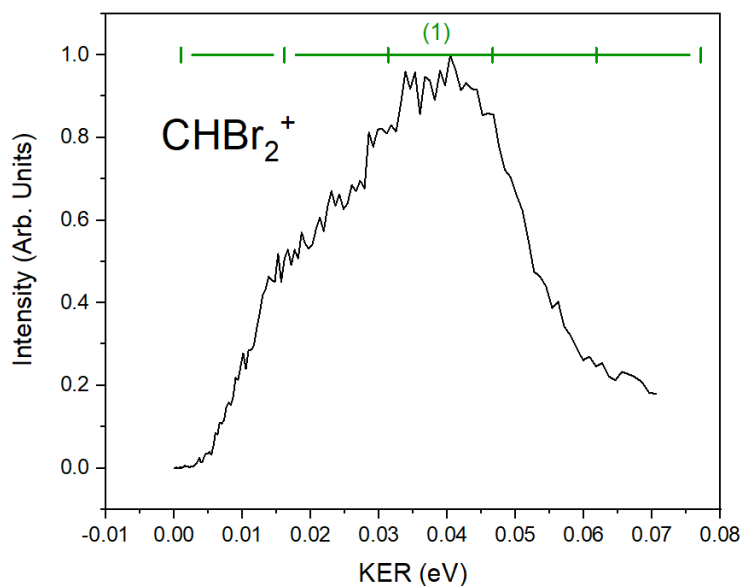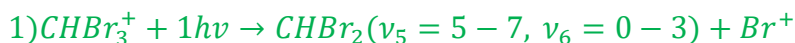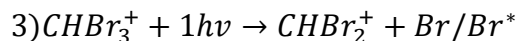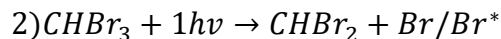

Figure 4.5 KER graph of CHBr$_2^+$.

The KER of the CHBr$_2^+$ was detected to be within the range of 0-0.07eV.

$$1)CHBr_3^+ + 1h\nu \rightarrow CHBr_2(\nu_5 = 5 - 7,\ \nu_6 = 0 - 3) + Br^+$$

Like CH$_2$Br$_2$ photodissociation's case, several processes have been determined not as active, based on the KER range of their corresponding products, the total number of photons required to obtain the detected radical, and whether the subsequent reactions following their products' dissociation result in more dissociation pathways. Accordingly, the following processes have been classified as less active.

$$2)CHBr_3 + 1h\nu \rightarrow CHBr_2 + Br/Br^*$$

$$3)CHBr_3^+ + 1h\nu \rightarrow CHBr_2^+ + Br/Br^*$$

Process 2) produces CHBr$_2$ radicals with kinetic energy of 0.77eV and 0.62 eV for the Br and Br* reactions respectively, far exceeding their detected KER range.

Similarly, process 3) produces $CHBr_2^+$ radicals with a kinetic energy of 1.46eV and 1.32 eV for the Br and Br* reactions respectively.
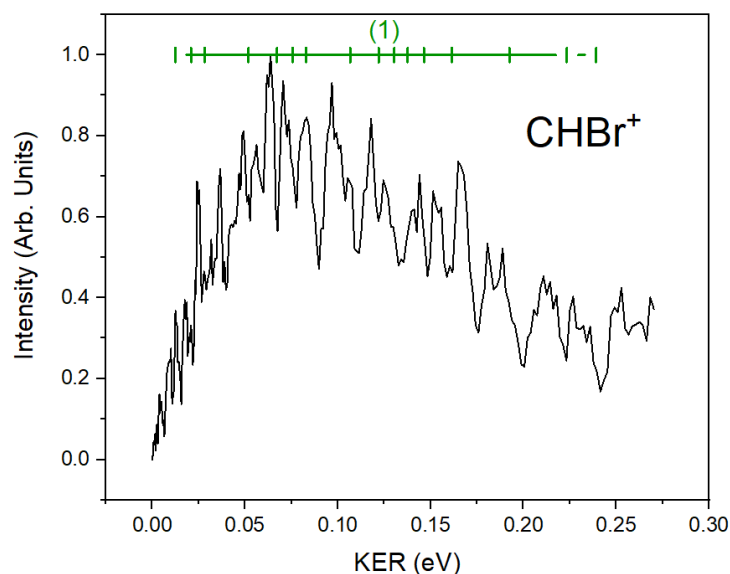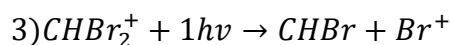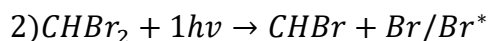

Figure 4.6 KER graph of $CHBr^+$.

The KER of the $CHBr^+$ was detected to be within the range of 0-0.27eV.

$$1) CHBr_2^+(v_5 = 0 - 3) + 1hv \rightarrow CHBr^+(v_1 = 1 - 4, v_2 = 0 - 3) + Br/Br^*$$

The $CHBr^+$ ion that was detected shows a relatively weak signal compared to the other ions, resulting in a low signal-to-noise ratio in the KER distribution. The reason behind the low signal from this specific ion can be attributed to its extensive dissociation, which gives rise to multiple photodissociation pathways, as will be showcased later.

The remaining possible photodissociation processes are considered less active. These processes are as follows:

$$2) CHBr_2 + 1hv \rightarrow CHBr + Br/Br^*$$

$$3) CHBr_2^+ + 1hv \rightarrow CHBr + Br^+$$

Process 2) produces CHBr radicals with a kinetic energy of 0.99eV and 0.77 eV for the Br and Br* reactions respectively.

Process 3) requires the $CHBr_2^+$ radical to be very highly internally excited for the dissociation to occur with a single photon.
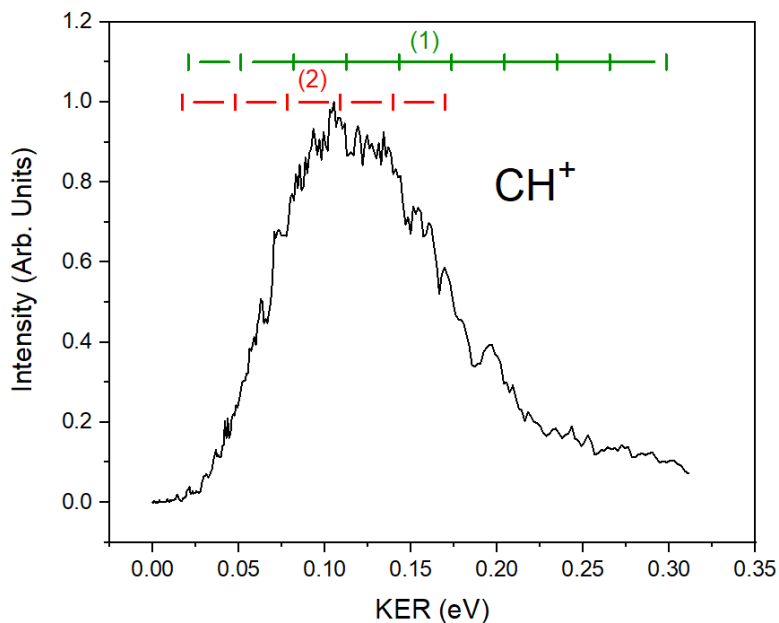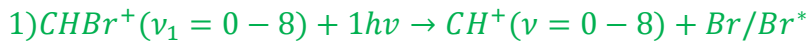

Figure 4.7 KER graph of CH^+.

The KER of the $CHBr^+$ was detected to be within the range of 0-0.31eV.

$$1) CHBr^+(v_1 = 0 - 8) + 1hv \rightarrow CH^+(v = 0 - 8) + Br/Br^*$$

$$2) CHBr^+(v_1 = 3 - 8) + 1hv \rightarrow CH(v = 0 - 3) + Br^+$$

The photodissociation of neutral CHBr was not found to give as active dissociation pathways as its corresponding ion.

Figure 4.8 KER graph of CBr⁺.

The KER of the CBr⁺ was detected to be within the range of 0-0.14eV.

$$1) CHBr^+(v_1 = 0 - 12) + 1hv \rightarrow CBr^+(v = 0 - 14) + H$$

$$2) CBr_2^+ + 1hv \rightarrow CBr^+(v = 14 - 17^{48}) + Br/Br^*$$

In process 1) we assigned as much internal energy to the CHBr⁺ as possible without breaking the compound, because this photodissociation reaction produces very cold (low KER) CBr⁺. This is due to the significantly lower mass of the H atom, which results in most of TKER being distributed to it, leaving CBr⁺ with a very small KER.

The reaction $CHBr^+ \rightarrow CBr + H^+$ requires 2 photons to occur.

Since the neural CBr fragment was not found to be produced (from the photoelectrons' KER distribution), we focus on the reactions resulting in CBr⁺.
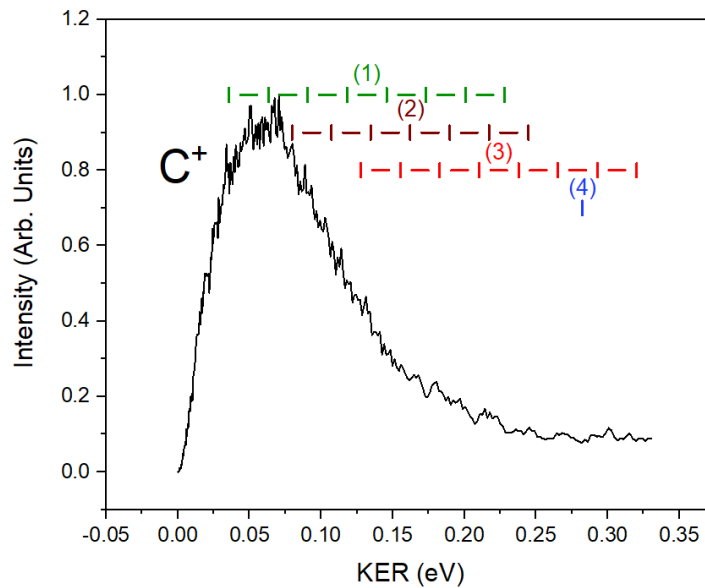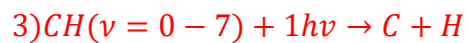
Figure 4.9 KER graph of C⁺.

The KER of the C⁺ was detected to be within the range of 0-0.33eV.

$$1) CH^+(v = 5 - 12) + 1hv \rightarrow C + H^+$$

$$2) CH^+(v = 0 - 6) + 1hv \rightarrow C^+ + H$$

$$3) CH(v = 0 - 7) + 1hv \rightarrow C + H$$

$$4) CBr^+ + 1hv \rightarrow C + Br^+$$

Process 4) is the only one of the photodissociation reactions of CBr/CBr⁺ that give C atoms with KER within the range detected.

Figure 4.10 KER graph of H⁺.

The KER of the H⁺ was detected to be within the range of 0-0.17eV

$$1) CHBr^+ + 1hv \rightarrow CBr^+ + H$$

$$2) CHBr_3 + 1hv \rightarrow CBr_3(v_3 = 7 - 10) + H$$

The internal energies of the compounds in process 1) have already been established.

The photodissociation reaction $CHBr_3^+ \rightarrow CBr_3 + H^+$ requires two photons to occur, while the $CHBr_3^+ + 1hv \rightarrow CBr_3^+ + H$ produces H radicals with kinetic energy exceeding 3.9eV.
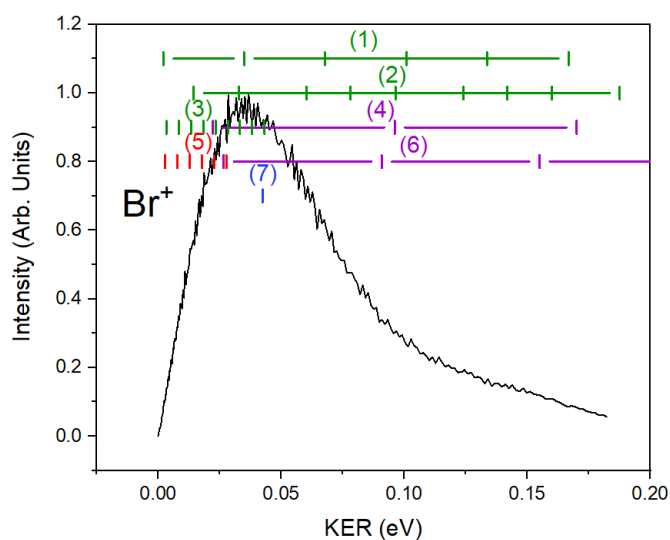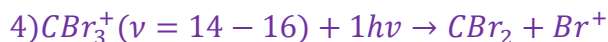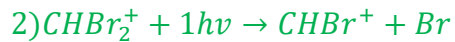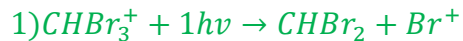

Figure 4.11 KER graph of Br⁺.

The KER of the Br^+ was detected to be within the range of 0-0.18eV

$$1) CHBr_3^+ + 1hv \rightarrow CHBr_2 + Br^+$$

$$2) CHBr_2^+ + 1hv \rightarrow CHBr^+ + Br$$

$$3) CHBr^+ + 1hv \rightarrow CH^+ + Br$$

$$4) CBr_3^+(v = 14 - 16) + 1hv \rightarrow CBr_2 + Br^+$$

$$5) CHBr^+ + 1hv \rightarrow CH + Br^+$$

$$6) CBr_2^+ + 1hv \rightarrow CBr^+(v = 14 - 17) + Br$$

$$7) CBr^+ + 1hv \rightarrow C + Br^+$$

The internal energies of the compounds of all the processes have already been established, except for 4) and 6).

Since the photoelectrons' KER graph shows large intensity of the photoelectrons obtained by the ionization of CBr_3 and CBr_2 fragments, we believe that the photodissociation of the ion fragments is a more active photodissociation channel.

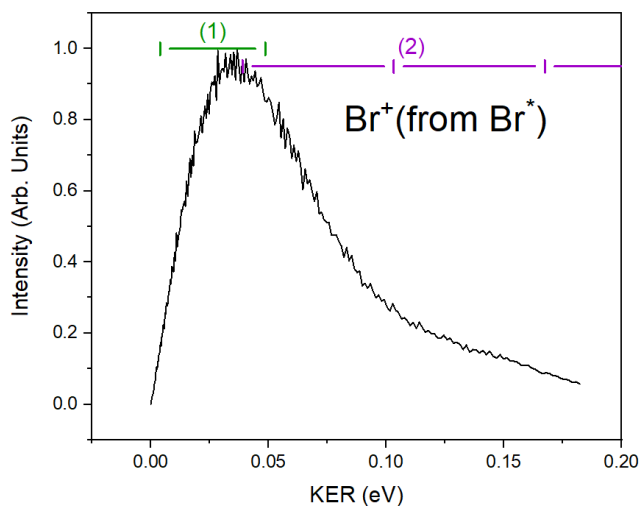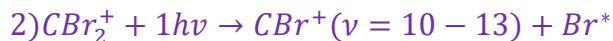Figure 4.12 KER graph of Br^+ produced by the ionization of Br*.

$$1) CHBr^+ + 1hv \rightarrow CH^+ + Br^*$$

$$2) CBr_2^+ + 1hv \rightarrow CBr^+(v = 10 - 13) + Br^*$$
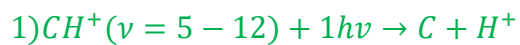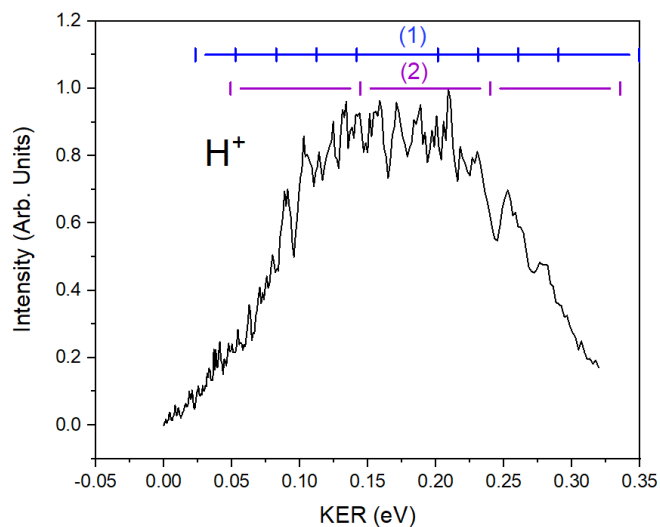
The internal energies of the compounds in process 1) have already been established.
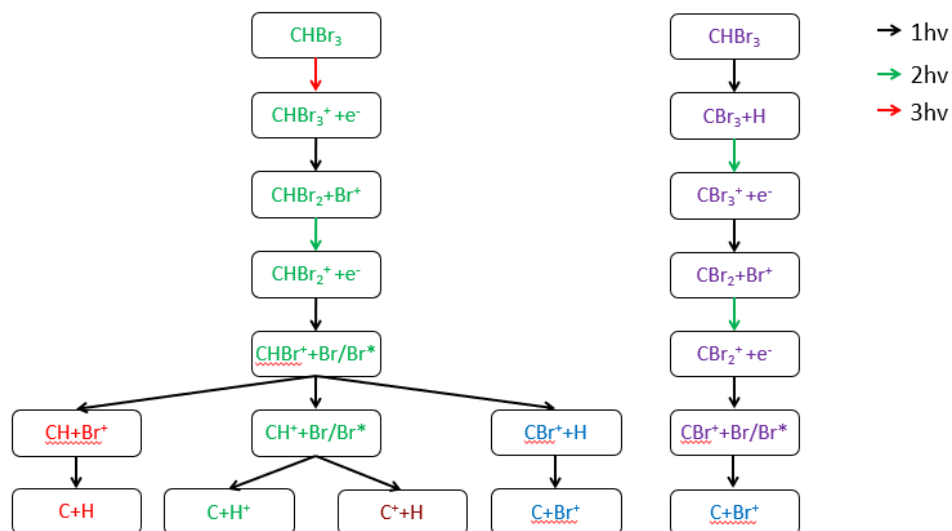
4.4 Conclusions

Figure 4.13 Photodissociation pathways' diagram.

Our findings indicate the existence of two significant photodissociation pathways. One pathway originates from the photodissociation of the neutral parent molecule, while the other pathway initiates from the photodissociation of the ion parent molecule, as depicted in Figure 4.13. Notably, the pathway on the left is primarily supported by the detected ion fragments, while the pathway on the right is primarily supported by the photoelectron signal.

Despite initially appearing unrelated, the signals obtained from the ions and photoelectrons distinctly uncover these two significant photodissociation pathways.

Furthermore, like the CH_2Br_2 photodissociation's case, our results effectively account for the entire observed KER range of the detected ion fragments, while also demonstrating that the photodissociation radicals are generated with high internal energy excitations.

References

1. Levine, R. D. (2009). *Molecular reaction dynamics*. Cambridge University Press.
2. Valeur, B., & Berberan-Santos, M. N. (2011). A brief history of fluorescence and phosphorescence before the emergence of quantum theory. *Journal of Chemical Education*, *88*(6), 731-738.
3. Atkins, P., Atkins, P. W., & de Paula, J. (2014). *Atkins' physical chemistry*. Oxford university press.
4. Hollas, J. M. (2004). *Modern spectroscopy*. John Wiley & Sons.
5. Foot, C. J. (2004). *Atomic physics* (Vol. 7). OUP Oxford.
6. Engel, T., & Reid, P. (2006). Physical Chemistry (edisi ke-6th).
7. Herzberg, G. (2013). *Molecular Spectra and molecular structure-Vol I* (Vol. 1). Read Books Ltd.
8. Whitaker, B. J. (Ed.). (2003). *Imaging in molecular dynamics: technology and applications*. Cambridge university press.
9. Zare, R. N., & Herschbach, D. R. (1963). Doppler line shape of atomic fluorescence excited by molecular photodissociation. *Proceedings of the IEEE*, *51*(1), 173-182.
10. Zare, R. N. (1972). Photoejection dynamics. *Mol. Photochem*, *4*(1), 1-37.
11. NIST, ChemistryWebbook. [http://webbook.nist.gov/chemistry/]
12. Marr, G. V. (Ed.). (2013). *Handbook on Synchrotron Radiation: Vacuum Ultraviolet and Soft X-ray Processes* (Vol. 2). Elsevier.
13. Scoles, G. (Ed.). (1988). *Atomic and molecular beam methods*. Oxford university press.
14. Ashfold, M. N., Nahler, N. H., Orr-Ewing, A. J., Vieuxmaire, O. P., Toomes, R. L., Kitsopoulos, T. N., ... & Parker, D. H. (2006). Imaging the dynamics of gas phase reactions. *Physical Chemistry Chemical Physics*, *8*(1), 26-53.
15. Imhof, R. E., & Read, F. H. (1968). A three-aperture electron optical lens for producing an image of variable energy but fixed position. *Journal of Physics E: Scientific Instruments*, *1*(8), 859.
16. Adams, A., & Read, F. H. (1972). Electrostatic cylinder lenses III: three element asymmetric voltage lenses. *Journal of Physics E: Scientific Instruments*, *5*(2), 156.
17. Abel, N. H. (1826). Auflösung einer mechanischen Aufgabe.
18. Chandler, D. W., & Houston, P. L. (1987). Two-dimensional imaging of state-selected photodissociation products detected by multiphoton ionization. *The Journal of chemical physics*, *87*(2), 1445-1447.
19. Eppink, A. T., & Parker, D. H. (1997). Velocity map imaging of ions and electrons using electrostatic lenses: Application in photoelectron and photofragment ion imaging of molecular oxygen. *Review of Scientific Instruments*, *68*(9), 3477-3484.
20. Gebhardt, C. R., Rakitzis, T. P., Samartzis, P. C., Ladopoulos, V., & Kitsopoulos, T. N. (2001). Slice imaging: A new approach to ion imaging and velocity mapping. *Review of Scientific Instruments*, *72*(10), 3848-3853.
21. Townsend, D., Minitti, M. P., & Suits, A. G. (2003). Direct current slice imaging. *Review of scientific instruments*, *74*(4), 2530-2539.
22. Papadakis, V., & Kitsopoulos, T. N. (2006). Slice imaging and velocity mapping using a single field. *Review of scientific instruments*, *77*(8), 083101.
23. Samartzis, P. C., Sakellariou, I., Gougousi, T., & Kitsopoulos, T. N. (1997). Photofragmentation study of Cl 2 using ion imaging. *The Journal of chemical physics*, *107*(1), 43-48.
24. Proch, D., & Trickl, T. (1989). A high-intensity multi-purpose piezoelectric pulsed molecular beam source. *Review of Scientific Instruments*, *60*(4), 713-716.
25. U. Brackmann, "Laser dyes," *Göttingen (Germany): Lambda Physik AG. D,* vol. 37079, 2000.
26. National Center for Biotechnology Information (2023). PubChem Compound Summary for CID 20531896, Dibromomethane;dichloromethane. Retrieved June 17, 2023 from https://pubchem.ncbi.nlm.nih.gov/compound/20531896.
27. Mehlmann, M., Quack, B., Atlas, E., Hepach, H., & Tegtmeier, S. (2020). Natural and anthropogenic sources of bromoform and dibromomethane in the oceanographic and biogeochemical regime of the subtropical North East Atlantic. *Environmental Science: Processes & Impacts*, *22*(3), 679-707.

28. Manley, S. L., Goodwin, K., & North, W. J. (1992). Laboratory production of bromoform, methylene bromide, and methyl iodide by macroalgae and distribution in nearshore southern California waters. *Limnology and Oceanography*, *37*(8), 1652-1659.

29. Molina, L. T., Molina, M. J., & Rowland, F. S. (1982). Ultraviolet absorption cross sections of several brominated methanes and ethanes of atmospheric interest. *The Journal of Physical Chemistry*, *86*(14), 2672-2676.

30. Kourtidis, K., Borchers, R., & Fabian, P. (1996). Dibromomethane (CH2Br2) measurements at the upper troposphere and lower stratosphere. *Geophysical research letters*, *23*(19), 2581-2583.

31. Schauffler, S. M., Heidt, L. E., Pollock, W. H., Gilpin, T. M., Vedder, J. F., Solomon, S., ... & Atlas, E. L. (1993). Measurements of halogenated organic compounds near the tropical tropopause. *Geophysical research letters*, *20*(22), 2567-2570.

32. Garcia, R. R., & Solomon, S. (1994). A new numerical model of the middle atmosphere: 2. Ozone and related species. *Journal of Geophysical Research: Atmospheres*, *99*(D6), 12937-12951.

33. Huang, J., Xu, D., Fink, W. H., & Jackson, W. M. (2001). Photodissociation of the dibromomethane cation at 355 nm by means of ion velocity imaging. *The Journal of Chemical Physics*, *115*(13), 6012-6017.

34. Sharma, P., Vatsa, R. K., Maity, D. K., & Kulshreshtha, S. K. (2003). Laser induced photodissociation of CH2Cl2 and CH2Br2 at 355 nm: an experimental and theoretical study. *Chemical physics letters*, *382*(5-6), 637-643.

35. Lee, Y. R., Chen, C. C., & Lin, S. M. (2003). Photodissociation of CH 2 Br 2, 1, 1-and 1, 2-C 2 H 4 Br 2 at 248 nm: A simple C–Br bond fission versus a concerted three-body formation. *The Journal of chemical physics*, *118*(23), 10494-10501.

36. Ji, L., Tang, Y., Zhu, R., Wei, Z., & Zhang, B. (2007). Photodissociation dynamics of CH2Br2 near 234 and 267 nm. *Spectrochimica Acta Part A: Molecular and Biomolecular Spectroscopy*, *67*(1), 273-280.

37. Long, J., Wang, H., & Kvaran, Á. (2014). Resonance-Enhanced Multiphoton Ionization of CH2Br2: Rydberg States, Photofragmentation, and CH Spectra. *The Journal of Physical Chemistry A*, *118*(10), 1826-1831.

38. http://garfield.chem.elte.hu/Burcat/burcat.html

39. NIST, Atomic Spectra Database. [https://www.nist.gov/pml/atomic-spectradatabase]

40. National Center for Biotechnology Information (2023). PubChem Compound Summary for CID 5558, Bromoform. Retrieved June 17, 2023 from https://pubchem.ncbi.nlm.nih.gov/compound/Bromoform.

41. Itoh, N., & Shinya, M. (1994). Seasonal evolution of bromomethanes from coralline algae (Corallinaceae) and its effect on atmospheric ozone. *Marine Chemistry*, *45*(1-2), 95-103.

42. McGivern, W. S., Sorkhabi, O., Suits, A. G., Derecskei-Kovacs, A., & North, S. W. (2000). Primary and secondary processes in the photodissociation of CHBr3. *The Journal of Physical Chemistry A*, *104*(45), 10085-10091.

43. Xu, D., Francisco, J. S., Huang, J., & Jackson, W. M. (2002). Ultraviolet photodissociation of bromoform at 234 and 267 nm by means of ion velocity imaging. *The Journal of chemical physics*, *117*(6), 2578-2585.

44. Huang, J., Xu, D., Francisco, J. S., & Jackson, W. M. (2003). Photodissociation of bromoform cation at 308, 355, and 610 nm by means of time-of-flight mass spectroscopy and ion velocity imaging. *The Journal of chemical physics*, *118*(7), 3083-3089.

45. Zou, P., Shu, J., Sears, T. J., Hall, G. E., & North, S. W. (2004). Photodissociation of bromoform at 248 nm: Single and multiphoton processes. *The Journal of Physical Chemistry A*, *108*(9), 1482-1488.

46. Tang, Y., Ji, L., Tang, B., Zhu, R., Zhang, S., & Zhang, B. (2004). Studies on photodissociation of alkyl bromides at 234 and 267 nm. *Chemical physics letters*, *392*(4-6), 493-497.

47. Yang, S. X., Hou, G. Y., Dai, J. H., Chang, C. H., & Chang, B. C. (2010). Spectroscopic investigation of the multiphoton photolysis reactions of bromomethanes (CHBr3, CHBr2Cl, CHBrCl2, and CH2Br2) at near-ultraviolet wavelengths. *The Journal of Physical Chemistry A*, *114*(14), 4785-4790.

48. Li, Z., & Francisco, J. S. (1998). High level ab initio molecular orbital study of the structures and vibrational spectra of CHBr+ and CBr+. *The Journal of chemical physics*, *109*(1), 134-138.